MEMS Spatial Light Modulator for Spectral Phase and Amplitude Modulation

By

Jonathan Dunayevsky

Thesis Supervisor

Dr. Dan M. Marom

Department of applied Physics
The Salim and Rachel Banin School of Computer Science and Engineering
The Faculty of Science and Mathematics
Hebrew University
Jerusalem
Israel

December, 2010

ABSTRACT

A diffractive Micro-Electro-Mechanical-system (MEMS) modulator is developed for modulating spectral components of incident light within the optical communication band. This diffractive MEMS spatial light modulator (SLM) is to be used for independently applying amplitude attenuation and phase control along one dimension. This enables a variety of applications for MEMS SLM devices such as channel selective attenuation, pulse shaping, chromatic dispersion compensation and more. The fabrication took place at Sandia National Laboratories where a predefined SUMMiT V process for MEMS designs exists. Furthermore, this fabrication process imposes constraints layer thicknesses. In addition two other constraints govern the design: the available voltage range (0-160 volts), and the need for the smallest mirror possible, due to the need of high resolution, were key factors in the design of the device. The electromechanical behavior of the device was well predicted using analytic calculation and FEA simulations. This thesis describes electrostatic technique and mechanical design features for realizing planar vertical travel in an electrostatically actuated diffractive optical device, which is robust, both to manufacture, and against pull-in. This device consists of many square elements, each 36 micron on a side. These elements act as reflective mirrors spanning a 2D rectilinear space with high fill factor. The mirrors can travel up to about 1.2 microns in the out-of-plane direction for applied voltage of 130 volts. The eigenfrequency of the device is about 24KHz.

תקציר

המאפנן הדפרקטיבי הוא מערכת מיקרן-אלקטרו-מכנית (MEMS) המתוכננת לאפנן רכיבים הספקטרלים בטחום הספקטרלי של התקשורת האופטית. המעפנן הספקטרלי הדפרקטיבי מאפשר בניפרד הנחתת מישרעת ושליטה על הפאזה של כל רכיב במימד אחד. למעפנן הספקטרלי מבוסס הממא"מ יכולים להיות ישומים שונים, כגון: הנחתת ערוצי תקשורת סלקטיבית, עיצוב פולסים, פיצוי נפיצה צבעית ועוד. ההתקן יוצר על ידי תהליך קבוע מראש ומעוצב במיוחד לבנית התקנית מהסוג הנ"ל בחברת "סנדיה נשיונאל לברטוריס". תהליך היצור הקבוע מראש שקובע עובי של כל שכבה הציב מגבלות על תכנון הרכיב. ישנם אילוצים נוספים, כגון מגבלת המתח שעומדת על 160 וולט והרצון לבנות מראה כמה שיותר קטנה (ככל שכל מראה קטנה יותר כך ניתן להשיג רזולוציה טובה יותר). לכל המגבלות הנ"ל היתה השפעה מכרעת על תכנון הרכיב. ההתכונות האלקרטו-מכניות של של המעפנן הדפרקטיבי נובאו בצורה אכותית על ידי סימולציות בשיטת finite element analysis (FEA). התאזה הנ"ל מתארת תכנון אלקטרוסטטית ועיצוב מכני מפורט אשר מאפשר יצור פלנרי של התקן עם יכולת תזוזה אנכית למישור הפלנרי של מערך יחידות דיפרקטיביות. כל יחידה כזו מהווה מראה, המראות הנ"ל פורסות מרחב דו-מימדי וממלאות אותו בצורה טובה. יכולת התזוזה של המראות היא יותר מ 1.2 מיקרון בהפעלת מתח של 130 וולט ותדר העצמי של יותר מ 24 קילוהרץ.

ACKNOWLEDGMENTS

I would like to take this opportunity to thank the many individuals who have contributed to my personal and academic growth over the past years culminating in the completion of this thesis.

First, I would like to thank my research supervisor, Doctor Dan M. Marom, who introduce me to and sparked my interest in optical communication technologies and MEMS devices. Dan have guided me through thesis and the research leading to it, has driven me to excel, and gave me the opportunity to work in this field.

I would like to thank the past and present members of the photonic devices laboratory, including David Sinefeld, Amitay Rudnick, Asael Adler, Dror Shayovitz, Yaron Glazer, Yoram Palti, Moran Bin Nun and Iska Fatal. Discussions with the members of the group have been insightful and helpful in many ways.

The members of Nano Fabrication Unit who have contributed greatly in the post-processing stage of my research.

Finally, I would like thank my parents Dmitry and Ludmila and my brother Boris for their never ending love and support.

TABLE OF CONTENTS

CHAPTER I

INTRODUCTION

MicroElectroMechanical Systems (MEMS) are used in a variety of fields, including optics, transportation, aerospace, robotics, chemical systems, biotechnology and microscopy. They are built using bulk or surface micromachining processes and are typically batch fabricated, similar to devices produced in the semiconductor industry.

MEMS are typically used in those fields either as sensors, which convert mechanical actions to output signals, or as active devices, which converts input signals to mechanical actions. This thesis deals with the second type.

1.1 MEMS THECHNOLOGY

An active MEMS device transfers energy from an input stimulus form into some type of displacement or mechanical response. Electrostatic actuation entails the application of a voltage difference to two conductors, which creates a force of attraction between the conductors and causes one or both of the conductors to move. Examples of this type of actuation are the Digital Micromirror Device (DMD) by Van Kessel [1] an electrostatic valve by Sato at.al. [2] and adaptive optical devices by Tuantranont et. al [3] and Bifano et. al. [4]. Thermal actuation exploits either a difference in the coefficient of thermal expansion (serpentine micro bridge by Judy [5] or polyimide bimorph actuators by Ataka [6]), or a temperature difference (an optical microactuator by Huja [7]), to cause bending. Piezoelectric actuation is generated by the application of an electric field across a piezoelectric crystal, ceramic, or a thin film. The converse piezoelectric effect [8] than induces a strain, which translates into a displacement (a large displacement pseudo-static actuator by Toshiyoshi [9] or a two dimensional micro scanner by Kawabata [10]). Magnetic actuation results from the force generated by a magnetic field; the fields are generally created passing a current through a surface coil (the actuators described by Toshyoshi [11], Liu [12] and Houlet [13]). Fluidic or pneumatic actuation generally refers to the use of fluidic under pressure to displace a flexible member (the balloon actuator by Kawai [14]).

Each actuation method has its strengths and weaknesses for different types applications. In addition to the desired magnitude of displacement, important metrics include speed, stability, size and ease of fabrication. Electrostatic actuation approach was chosen because it can be very fast, stable readily integrated with existing fabrication technology, and designed to generate various types of displacement. Thermal actuators are limited in vertical or lateral displacement, but generate large force, so are more suited to cause bending displacement. Piezoelectric actuators generally displace by a small amount, and so they are better used to generate bending rather than vertical displacement. Large vertical travel using piezoelectric actuation typically requires excessively complicated fabrication processes or large voltages, since the displacement scales with voltage and size of the device. Magnetic actuators often require large die area since they require coils. Fluidic actuators are typically large and relatively slow.

1.2 OPTICAL MEMS DEVICES

MEMS are revolutionizing the field of optics. MEMS structures are suitably sized to interact well with light in reflective configurations such as the Texas Instruments Digital Micromirror Device (DMD) [15] or in diffractive configurations such as the Silicon Light Machines Grating Light Valve [16]. When the reflective approach is implemented, the optical system external to the MEMS device determines the motion required by the device. When the diffractive approach is implemented, the motion required by the MEMS device is typically on the order of the incident wavelength. The device described in this thesis is intended for optical communication applications which means that typical wavelength is around 1550nm.

For optical applications there are four main categories of devices categorized by their type of motion: flip-up, torsion, planar, and lateral. Flip-up mirrors are used for optical benches (Lin [17]). Torsion mirrors are used to process light in reflective applications (optical add-drop switching by Ford [18]) or in displays (such as TI DMD [1]) which is particularly suited to closely spaced arrays and where light is routed dependent on mirror orientation. Vertical planar displacement of small elements allows diffractive applications or adaptive optics [16] for example). Lateral displacement MEMS can be used to build devices such as varying period gratings (demonstrated by Chen [19]).

1.3 SPATIAL LIGHT MODULATOR

A spatial light modulator (SLM) is an object that imposes some form of spatially-varying modulation on a beam of light. A simple example is an overhead projector transparency. In optical communication SLMs are used for variety applications. Such as Pulse shaping [22], chromatic dispersion compensation [23],[25], wavelength selective switching [24], and more. There are several methods of implementing an SLM. SLMs can be created with liquid crystal technology [20], [21] or MEMS technologies such as the Texas Instruments Digital Micromirror Device [1], interferometric devices such as the Stanford Grating Light Valve [16]. There are several advantages of MEMS technology over the liquid crystal SLMs. First, liquid crystal SLM requires that the input light be linearly polarized, necessitating the use of polarization diversity when the state of polarization cannot be controlled (as in telecom). MEMS micromirrors are polarization insensitive. Second, liquid crystal has response time of about a millisecond. MEMS devices, especially the diffractive MEMS variety that actuate to a fraction of an optical wavelength, can be designed to operate much faster. The main disadvantage of the

MEMS in comparison to the liquid crystal, is that MEMS devices usually in need of high voltage sources for operation while liquid crystal technology do not.

1.4 THESIS OUTLINE

In the present chapter, different types of MEMS are presented as background for this thesis. A survey of different type and applications for optical MEMS is presented as well. The concept and theory of operation of this device is described along with possible applications.

Chapter 2 presents the parameters and constraints affecting device design and the simulations used to demonstrate the functionality of the device. A simplified analytical model along with Finite Element Analysis (FEA) model is used to simulate device design and predict the performance of the device.

The fabrication of the device is discussed in Chapter 3, encompassing device layout and the process flow, and is illustrated using 3D illustrations. Postprocessing challenge including metallization and packaging are addressed. The result of the fabrication process is then presented.

The experimental results of this thesis are presented in Chapter 4. The electromechanical characterization parameters from direct measurements are presented and compared to simulations from Chapter 3. Methods for optical characterization are discussed and illustrated. Different optical measurements are presented to demonstrate the functionality of the device for different telecom applications.

In Chapter 5 the work presented in this thesis is summarized.

1.5 THE DIFFRACTIVE MEMS SLM

The primary goal of this thesis is to design and test a MEMS Spatial Light Modulator (SLM). This diffractive MEMS modulator is intended for modulating spectral components of spatially dispersed incident light.

Fig.1.1 shows a simplified typical configuration that is used to project the dispersed light to the SLM and couple it back into the optical fiber. The configuration uses an optical circulator at the light input/output port. The light emerging from the fiber passes through a dispersive element (diffraction grating or arrayed waveguide grating) and is projected on the SLM.

Due to dispersion in the element each channel falls on a different place on the SLM (liquid crystal or MEMS). The light is manipulated on the SLM and then reflected and coupled back into the optical fiber and out of the system through the circulator out port.

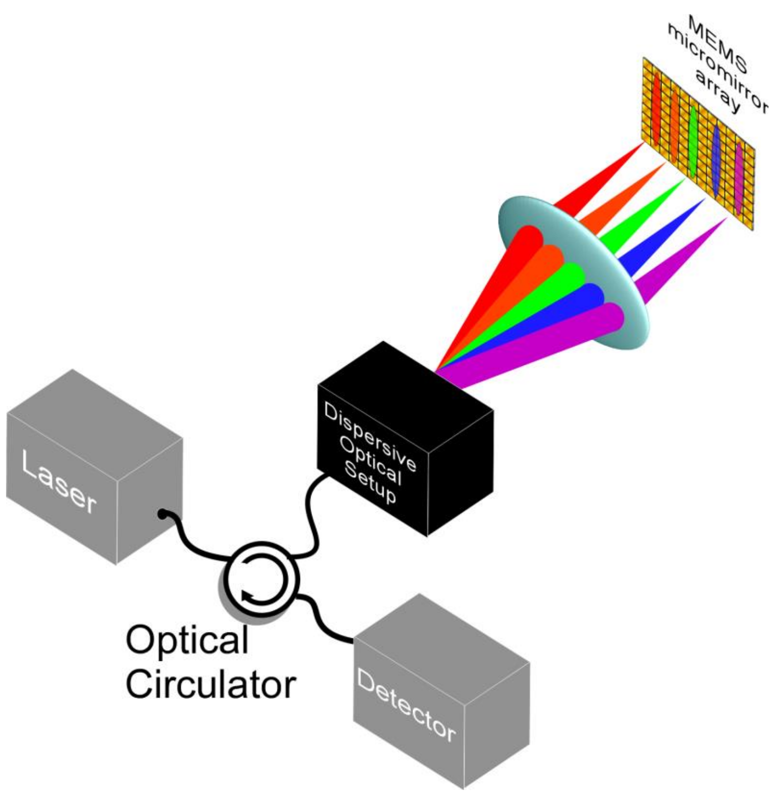

Fig.1.1 Typical SLM setup

Most SLMs works almost exclusively in either phase or amplitude modes, not both. However for telecom filtering applications it would be desirable to set arbitrary spectral amplitude and phase response across the signal bandwidth.

(a)

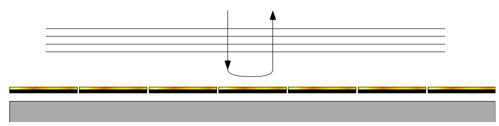

(b)

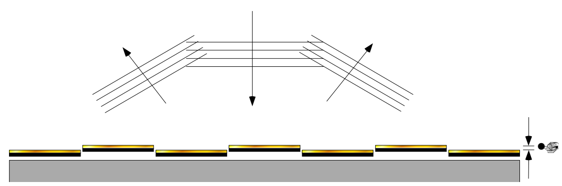

Fig1. 2. Schematic diagram of single channel attenuation. No sag, reflection (a), respective sag of $\lambda/4$, Diffraction (b)

The basic principle for a single channel attenuation is based on an already proven concept developed by David M. Bloom technology [16] (illustrated in Fig1.3). Bloom's diffractive MEMS modulators have been based on slender reflective strips, half of which are fixed and the other half movable arranged alternately. The movable half can be set be set anywhere from fully in phase to fully out of phase with the fixed half (Fig1.2), achieving a controlled degree of interference. With no voltage applied (Fig1.2(a)) on the movable strips the light is reflected to the incident direction. With voltage applied (Fig1.2(b)) on the movable strips, those strips are pulled down a quarter wavelength. That creates a total path-length difference between the light reflected from the movable strips and the fixed strips of half a wavelength and thus reflection interferes destructively and no light is reflected to the incident direction. In this case the incident light is diffracted into higher-order diffraction modes. A spatial filter blocks the diffraction orders, and the amplitude (or energy) of the zero order term can thus be fully modulated. Our new diffractive MEMS modulator for both amplitude and phase control enables independent motion of the two diffractive halves. Fig1.3 shows schematically the periodic phase delay associated with the two interleaved reflective mirror set. One reflective mirror is set to provide a ϕ_1 phase delay, whereas the second provides a ϕ_2

phase delay. The complex amplitude, zero order diffraction term is $\frac{1}{2}\left(e^{j\phi_1}+e^{j\phi_2}\right)$, which can be further simplified to

$\cos\left(\frac{\phi_1-\phi_2}{2}\right)\times e^{j\frac{\phi_1+\phi_2}{2}}$. Therefore, the phase average between the two reflective mirrors determines the reflected phase and the phase difference between the two reflective mirrors determines the amplitude to the zero order diffraction. In order for the modulator to continuously impose any phase within [0,2π] and any amplitude within [0,1], each reflective mirror should be capable of modulating continuous phase within [0,2π]. Since the phase delay associated with the mirror displacement is twice the mirror travel, the mirror sag should be controlled within the range of 0 to 800 nm for optical communication wavelengths (around 1550nm). The new diffractive MEMS modulator utilizes two individually controlled sampled mirrors, as opposed to reflective strips of Bloom's diffractive MEMS modulator. Additionally, the orientation of sampling is not in the spatial dispersion direction, but orthogonal to it. The orientation change creates fixed width pixels in the dispersion direction, where the complex amplitude of each pixel can be set.

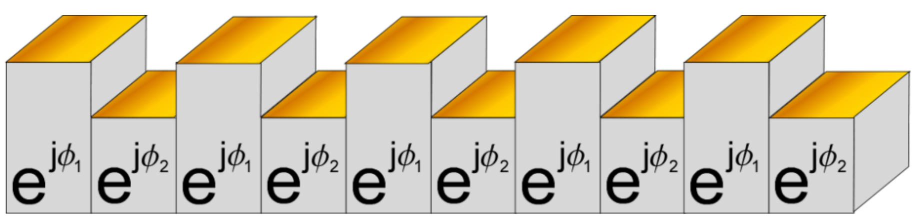

Fig1. 3 Periodic phase modulation with adjustable values ϕ_1 and ϕ_2, forming the basis of the amplitude and phase diffractive MEMS modulator.

The basic concept of operation of the SLM in this thesis is as follows: The modulator contains pixels spanning a 2D rectilinear space (Fig1.4) with high fill factor, however each column of the array is an independent module. All even and odd pixels of a column are attached to their own actuators which are hidden beneath the mirrors and actuated independently.

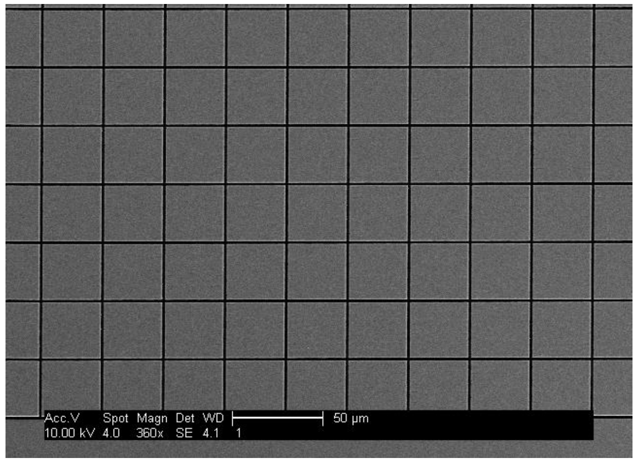

Fig 1.4. Scanning electron micrograph of the two dimensional mirror array

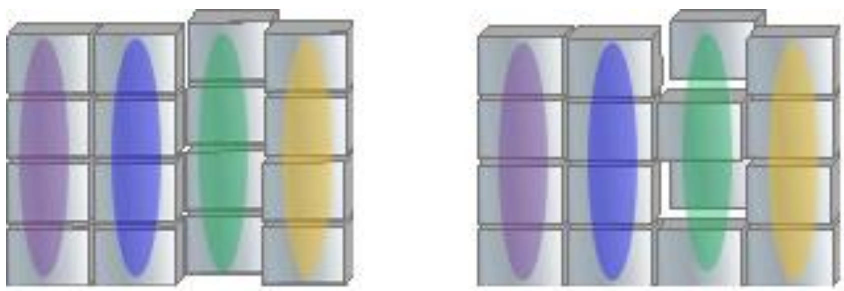

Fig1.5.(a) Mutual displacement (Left), Respective displacement (Right)

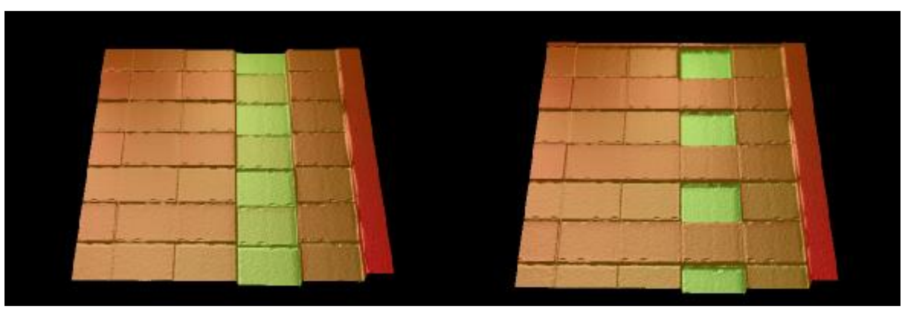

Fig1.5.(b) Mutual displacement (Left) and respective displacement (Right).
Images are taken by WYKO interferometric microscope.

All the even mirrors are attached to one beam and all the odd mirrors are attached to the other. These beams are part of the actuator that pulls in towards the substrate, pulling along the mirrors with them. Mutual displacement (Fig1.5 (Left)) of the mirrors in the column controls the phase upon reflection (with half a wavelength sag it is possible to imply each spectral component with any phase from 0 to 2π), while the relative position(Fig1.5 (Right)) of the mirrors can give constructive through destructive interference patterns (as discussed in previous part), thus controlling the amplitude of each spectral component. While the relative mirror displacements can be used as channel selection manipulation, the mutual displacement of each column's mirrors is useful for manipulating the phase of each spectral component independently (for example in chromatic dispersion compensation or pulse shaping applications).

CHAPTER II

DESIGN AND MODELING

In order to manipulate a spectrum in the convensional in the optical communication wavelengths (c-band) the mirrors should travel at least half of the maximum wavelength in the c-band, about 800nm. There are three main constrains on the design: the available voltage range, predetermined fabrication process and the desired mirror size. The type of electronics that was used limits the voltage range to 160volts. The fabrication process that was used is a commercially available SUMMiT V process offered by Sandia National Laboratories. The size of the mirror (or pixel) will determine the resolution of the device. The pixel should be as small as possible and yet fully cover a two dimensional space. To allow small periodic mirrors the actuators underneath them should be compact. This compactness is limited by the fabrication process since the minimum feature in the process is limited to 1μm and the misalignment tolerance between the layers is 0.5μm. In this chapter the electro-mechanical coupling problem will be analytically studied, design considerations will be described and discussed.

2.1 ANALYSIS OF ELECTRO-MECHANICAL COUPLING

In order to understand the typical behavior of this sort of systems, a reference problem is considered as shown in Fig. 2.1. It consists of a capacitor made of two parallel and perfectly conducting discs between which a voltage is applied. The upper disc is moveable and is held by a spring while the lower disc is fixed. For sake of simplicity, the electrodes of the capacitor are considered to be infinite planes, and the electric charge is evenly distributed on the surface. The stiffness is also assumed to be distributed over the upper electrode.

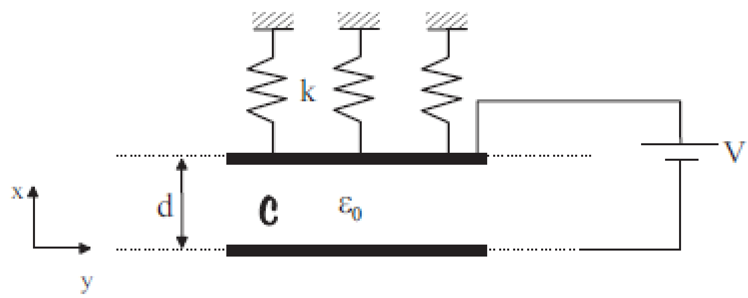

Fig. 2.1 Definitions of the reference problem

The equation of motion that has to be solved is:

$$m\ddot{d} = -k(d - d_0) - \frac{\varepsilon V^2}{2d^2} \qquad (2.1)$$

Where m is the mass of the moveable plate, V is the applied voltage, d is the gap between the electrodes, d_0 is the initial gap between the electrodes, k is the stiffness of the spring and ε is the dielectric constant of the surrounding medium. For the problem that will be shown here, we use a quasi-static analysis, i.e. $\ddot{d} = 0$. Hence the equation is reduced to:

$$-k(d - d_0) - \frac{\varepsilon V^2}{2d^2} = 0 \qquad (2.2)$$

The total stiffness of the structure resulting from the coupled problem is obtained by differentiating the static force (f) (2.2) with respect to the displacement for an equilibrium position d_e :

$$\left[\frac{\partial f}{\partial d}\right]_{d=d_e} = -k + \frac{\varepsilon V^2}{d_e^3} \qquad (2.3)$$

Expression (2.3) may be considered as an effective stiffness of the system. It can be seen that the electrostatic force can introduce in the system negative effective stiffness that increases as the distance between the electrodes decreases. The voltage for which coupled stiffness equals to zero called "static pull-in voltage". The pull-in voltage:

$$V_{PI} = \sqrt{\frac{k d_e^3}{\varepsilon}} \qquad (2.4)$$

Pull-in voltage is the maximum voltage that can be applied on the lower electrode for the system to remain stable. If a voltage higher than the pull-in voltage is applied to the system the coupled stiffness of the system will be negative. To determine the maximum d_e equation 2.2 is used. Since V_{PI} is the maximum voltage that can be applied:

$$\left[\frac{\partial V}{\partial d}\right]_{d=d_e} = \frac{\partial}{\partial d}\left(\frac{2k}{\varepsilon} d^2 (d_0 - d\right)^{1/2} = \frac{1}{2} \left(\frac{2k}{\varepsilon}\right)^{1/2} \frac{(2d_0 - 3d)}{(d_0 - d)^{1/2}} = 0 \qquad (2.5)$$

It can be seen that the equation is satisfied for $d_e = \frac{2}{3} d_0$. If that is applied to equation 2.4:

$$V_{PI} = \sqrt{\frac{8kd_0^3}{27\varepsilon}} \qquad (2.6)$$

The following dimensionless graph (Fig. 2.2) is showing the behavior of that system:

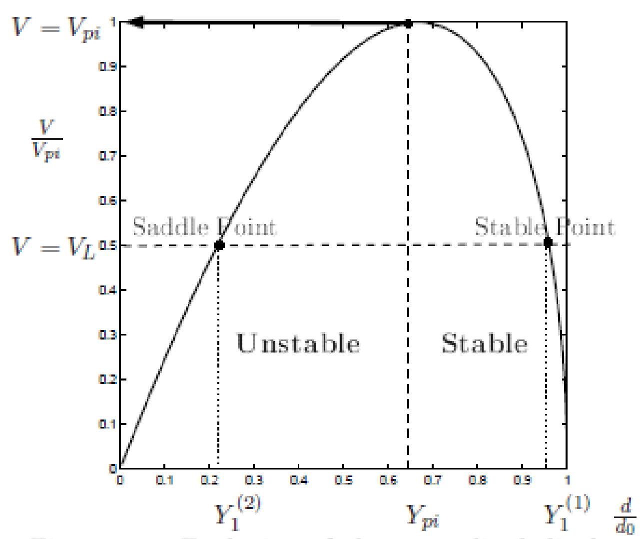

Fig. 2.2 Evaluation of the normalized displacement with normalized the voltage

If the system goes to the unstable region the upper electrode will go all the way to the lower electrode. The Vander-Waals attractive force will stick the two electrodes together and since there is no repelling force that can be applied, the structure will remain stuck. Stiction problems are very common in this type of systems and have to be taken it in consideration in the design.

In conclusion this short analysis shows that if the mirror has to travel 800nm, the gap between the plates has to be at least three times the required displacement, or 2.4µm.

2.2 DESIGN CONSIDERATIONS

2.2.1 Supporting Beam for the Mirrors

In order to allow the simultaneous movement of all the even (or odd) mirror of the same column, all those even (or odd) mirrors have to be attached to the same beam. Since we want long arrays of small mirrors, those beams should be long and narrow. Those beams are also required to be stiff, such that there is minimal flexing and the mirrors remain on the same plane. If the requirement is to be satisfied, the supporting beams can no longer be long plates. The beams must be much stiffer structures. U-shaped beams (Fig. 2.3) were designed in the actuator region to make the mirror supporting beam much stiffer. In addition the mirrors were attached in two spots. This toughens the structure even more, since the springs are always attached to the boxy regions. Finally it was decided to support each beam by multiple "legs", much like a centipede, that attempt to spread the load and the forces acting on the beam.

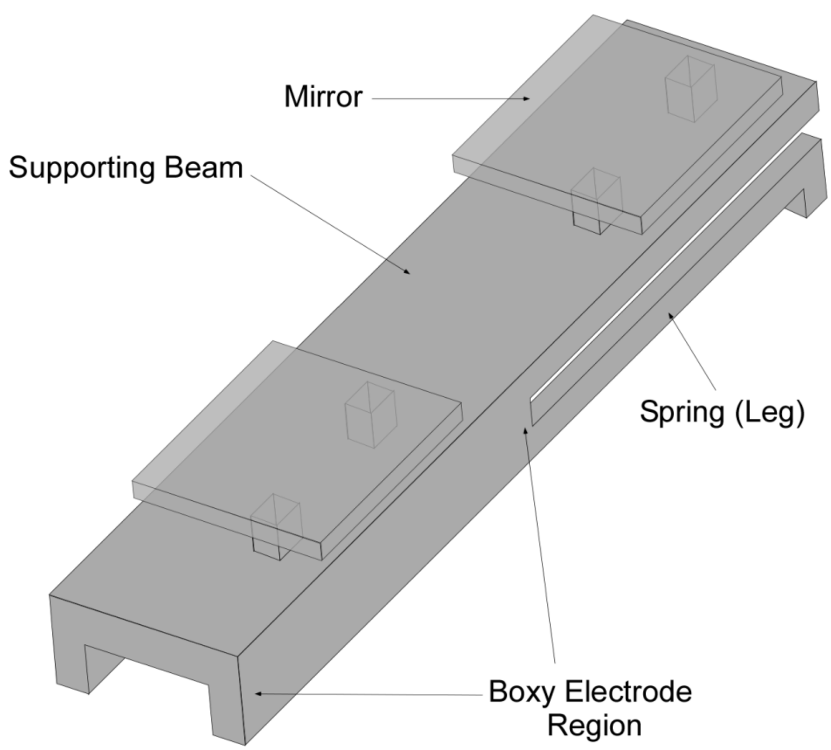

Fig. 2.3 The supporting beam design.

2.2.2 Spring Parameters Considerations.

The "legs" act like flexure beams. Each spring (leg) is fixed on left end of the substructure and preserves a zero angle at the right end (actuator side). This is an analogous to the problem presented in Fig. 2.4. The spring constant corresponding to the elastic interaction between the force F_{1z} and the resulting deflection u_{1z} can be found.

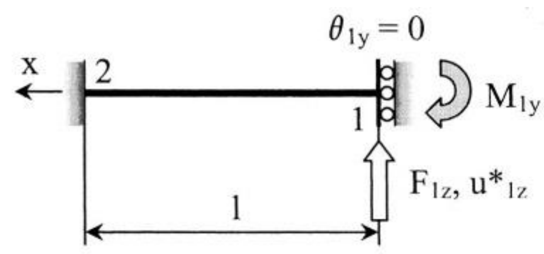

Fig. 2.4 Spring force diagram.

The spring constant corresponding to the elastic interaction between the force F_{1z} and the resulting deflection u_{1z} can be found.

We can then write the displacement the following way:

$$\begin{cases} u_{1z} = C_{1,uz-Fz}F_{1,z} + C_{1,uz-My}M_{1,y} \\ \theta_{1,y} = C_{1,uz-My}F_{1,z} + C_{1,\theta z-My}M_{1,y} \end{cases} \tag{2.7}$$

For free-guided beam we demand $\theta_{1y} = 0$.

$$M_{1,y} = -\frac{C_{1,uz-My}}{C_{1,\theta z-My}} F_{1,z} \tag{2.8}$$

From the equation for u_{1z} we get:

$$K_{1,Fz-uz} = \frac{F_{1,z}}{u_{1,z}} = \left(C_{1,uz-Fz} - \frac{C_{1,uz-My}^2}{C_{1,\theta z-My}}\right)^{-1} \tag{2.9}$$

Using the compliances for the constant cross-section fixed-free beam:

$$\begin{cases} C_{1,uz-Fz} = \dfrac{l^3}{3EI_y} \\ C_{1,uz-My} = \dfrac{l^2}{2EI_y} \\ C_{1,\theta z-My} = \dfrac{l}{EI_y} \end{cases} \qquad (2.9)$$

Where E is young's modulus, l is the length of the beam, I_y is the cross-sectional moment of inertia, for rectangular cross-section $\left(I_y = {w \cdot t^3}/{12}\right)$

Here w and t are the width and the thickness of the beam.

We can calculate the spring stiffness K for this beam.

$$K_{1,Fz-uz} = \frac{F_{1z}}{u_{1z}} = \frac{12EI_y}{l^3} = \frac{Ewt^3}{l^3} \qquad (2.10)$$

The three constrains that were mentioned at the beginning of the chapter are determining the spring parameters. First of all the spring is constructed in a 1µm thick layer, because that is given in the predetermined process. The second consideration is the width of the spring. On one hand, the spring should be as thin as possible to make the structure compact. On the other hand, sideways movement of the structure should be minimized. To prevent the sideways movement of the structure, the width of the spring should be at least twice the thickness, this way the stiffness in the up-down direction is four times weaker than the stiffness for sideways direction. Hence the width of the spring is determined to be 2 µm. To determine the length of the spring the maximum voltage constrain should be considered. I took a safety margin and set the pull-in voltage to be 100volt. Since electrical shielding have to be set (Will be discussed later in this chapter) the effective pulling area has to be set on about half of the electrode area. I set it to be

$400\mu m^2$ because this is approximately the area of the electrode underneath an area that is supported by two springs. The parameters are later fine tuned by FEA simulations.

$$V_{PI} = \sqrt{\frac{8kd_0^3}{27\varepsilon A_{eff}}} \qquad (2.11)$$

Where A_{eff} is the effective pulling area.

Since the initial gap d_0 is determined by the process to be 3.8µm, the maximum stiffness is calculated to be $K_{max} = 2.16\, {}^{N}/_{m}$. Two springs have to be attached to each actuator for stability considerations, which means that the maximum stiffness of each spring is $1.08\, {}^{N}/_{m}$. From equation 2.10 the minimum length of the spring is calculated to be about $70\mu m$.

2.2.3 Actuator Considerations.

Two types of actuators were designed and fabricated. Both designs (Fig. 2.5) have an I-shaped electrode underneath the actuator. Design(A) has a wider electrode than design(B). In design(A) the electrode doesn't lay underneath the entire structure, but only under the boxy parts where there are no springs. The electrodes in design(A) are connected between them by thin wires in the spring regions. These thin wires lay between the two springs and covered by a shielding tunnel (Electric shielding will be discussed separately in this chapter). Wide electrodes are possible since there is no need in extra width for the springs. Wide electrodes in design(A) are better in process misalignment issues than in design(B), since the actuator acts very much like parallel plate actuator. The mirror supporting beam in design(A) is not as stiff as in design(B) but should be enough to keep the mirrors leveled. In design(B) the electrode is laying underneath the entire structure. In design(B) the electrode is narrower than is design(A) but can generate the same amount of power as in design(A), since it has the same effective area.

To calculate this affective area, Comsol simulations were made using spring stiffness that have been calculated earlier. The simulation (Fig. 2.6) is a 2D simulation where the third dimension is taken into account, but cannot be seen. That simulation demonstrates the displacement of the actuator for an applied voltage. A right half of an actuator is show in Fig. 2.6 , but the calculations take in account that there is a symmetric left half. The black line represent the original location of the actuator, while the red line shows the displaced location due to an applied voltage. In the same simulation the surface colors represent the electric field. This way the quality of electric shielding may be determined.

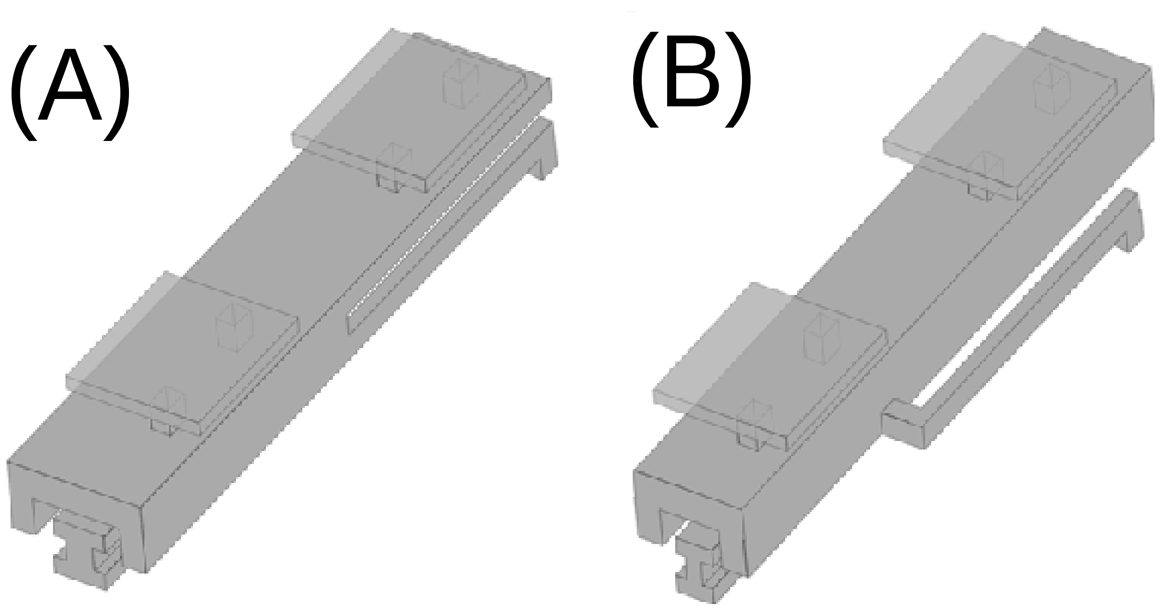

Fig. 2.5 Two actuator designs. Each consists of an I-shaped electrode and U-shaped mirror supporting beam. Design(A) is on the left and design(B) is on the right.

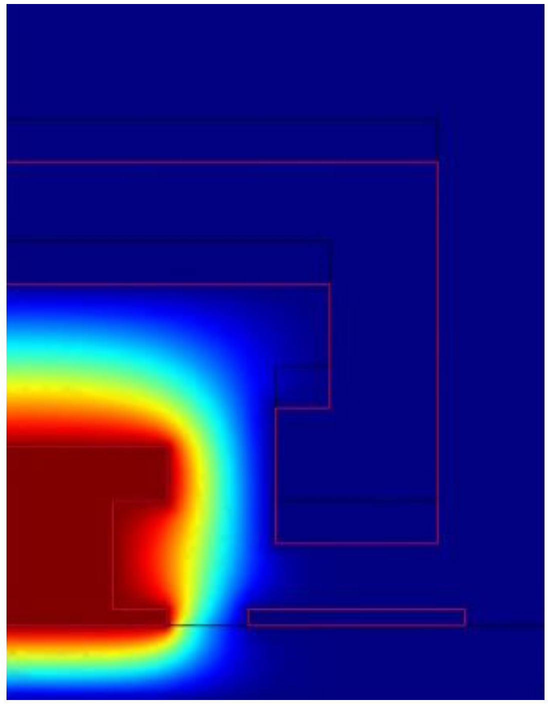

Fig. 2.6 An electrostatic Comsol simulation of the actuator of design(A)

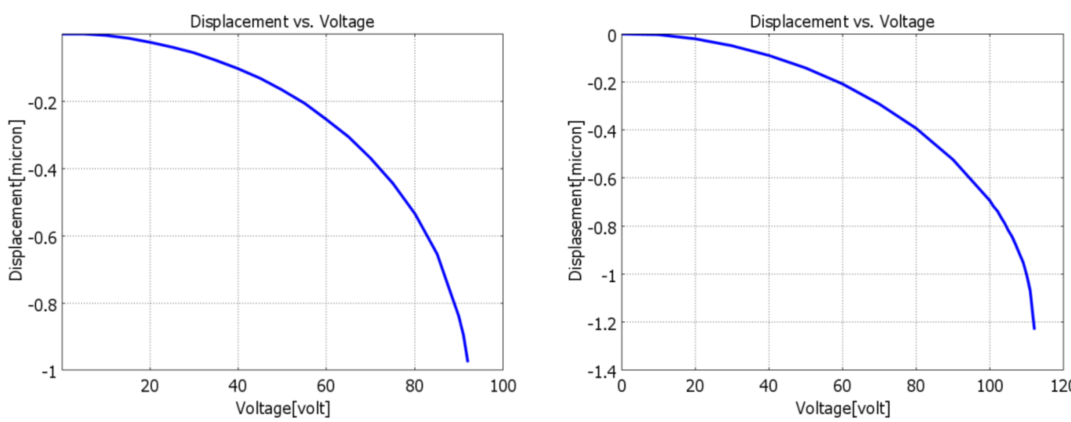

Fig 2.7. Graphs showing the displacement that occurs due to applied voltage. The displacement versus voltage for design(A) on the left and for design(B) on the right.

Fig. 2.7 shows the displacement of the actuator dependence on the applied voltage for both designs. The last point in each graph shows the pull-in voltage. It can be clearly seen from the graphs that the voltage that has to be applied in order to displace the actuator 800nm, is not significantly smaller then the pull-in voltage. In order to recede the pull-in voltage from the working region, according to equation 2.11, either the stiffness of the spring or the gap has to be increased. Both those changes would also increase the voltage that is needed for the 800nm displacement. The solution was to create a nonlinear spring that has low stiffness coefficient for displacement of 0- 850nm and high stiffness coefficient for 850nm and above. The way to do so is by creating a small dimple (Fig. 2.8, white) on the bottom of the spring.

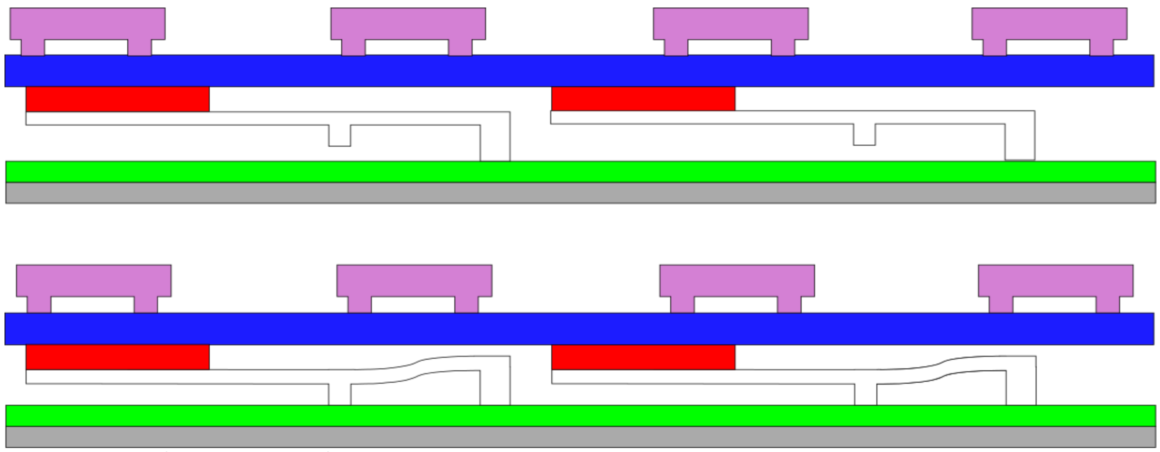

Fig 2.8. Sketch of a cross-section of design(A) along the spring. The upper diagram is the structure with no voltage applied. The lower diagram is the structure with voltage above 100volts applied.

This gap between the dimple and the underneath polysilicon layer is 0.5µm. The dimple is inactive while the displacement is smaller than 0.9µm and the spring acts as described earlier. When the displacement is larger than 0.9µm, the dimple touches down and effectively shortens the spring. Now the effective length of the spring is half of what it was before the dimple touched down and according to equation (2.10) the stiffness of the spring rises to about eight times the original stiffness. In Fig, 2.9 shown the displacement of the actuator dependence on the voltage that is applied. This simulation shows that with an addition of the dimple, voltage up to 400volts can be applied with no concern of snap-down and sticktion.

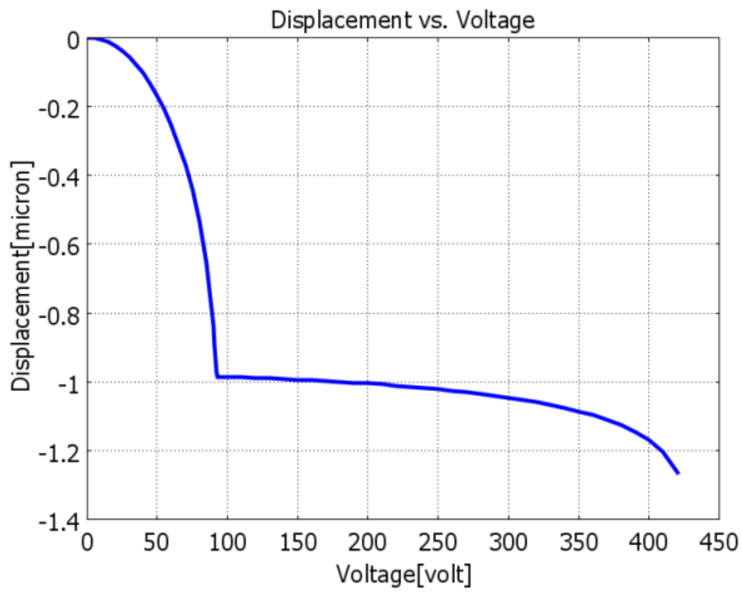

Fig 2.9. The displacement versus voltage for design (A) with the addition of the dimple.

2.2.4 Electrical Shielding Considerations.

Electrical shielding is a crucial issue in the designs. The interaction between an electrode and a neighbor actuator, or electrical crosstalk, is undesired. In addition no electrostatic force should be applied directly on the springs. Even a relatively small force that is applied directly on the springs will cause downward or sideways displacement. As shown in Fig. 2.5 the actuators are designed to act as dynamic electric shields. As higher voltage is applied to the actuator, the u-shaped actuator is pulled down and less gap remains between the actuator and the underneath grounded layer, increasing the shielding it provides. This way the shielding is in a way dynamically adjusted to the applied voltage. Fig. 2.6 shows the electric field distribution in the electrode region. It can be clearly seen that outside the actuator the electric field is zero and no interaction with neighbor actuator is expected.

The second issue is that the process impose that the structure is composed on a thin dielectric layer of silicon nitride. A grounded layer has to be deposited directly on the silicon nitride as close as possible to the electrode, otherwise when high voltage is applied the dielectric layer traps electric charges and after the voltage is turned off those charge would apply some unwanted force.

The third issue is that in design (B) the springs are always shielded by the dynamic shielding of the u-shaped actuator, while in design(A) the electrodes connected with thin wires that pass close to springs. Electric shielding tunnel was designed to prevent for the wires electrically interact with the springs.

CHAPTER III

FABRICATION

The fabrication process for the MEMS SLM is described in this chapter. 3D sketches and mask layouts describe the process flow, illustrate the combination of the masks and process steps used to create the device. Only the design process flow of (a) is shown in this chapter since there are very small fabrication differences between designs (a) and (b). The metal layer that is offered for bond pads metallization does not suit for mirror metallization, that is why a custom process to metalize the mirrors after the structure release was designed. This custom process is described in the post processing section of this chapter. The last section of this chapter describes the packaging.

3.1 FABRICATION PROCESS OVERVIEW

The fabrication process we used is a commercially available process called Sandia Ultra-planar Multi-layer MEMS Technology V (SUMMiT V) offered by Sandia National Laboratories. SUMMiT V is a 1.0 micron, 5-level, surface micromachining (SMM) technology featuring four mechanical layers of polysilicon above a thin highly doped polysilicon electrical interconnect and ground plane layer. Sacrificial oxide is sandwiched between each polysilicon level. The thin sacrificial film defines the amount of mechanical range of motion. The oxide layer directly beneath the upper two layers of mechanical polysilicon are planarized using a chemical mechanical polishing (CMP) process. The entire stack shown below in figure 3.1, is fabricated on a 6-inch single crystal silicon wafer with a dielectric foundation of 630nm of thermal oxide and 800nm of nitride. The layers of polysilicon are designated from the substrate up as MMPOLY0 through MMPOLY4 ("MM " stands for micromechanical). The sacrificial films are designated as SACOX1 through SACOX4, with numerical suffix corresponding to the number of the subsequent layer of mechanical polysilicon that is deposited on a given oxide.

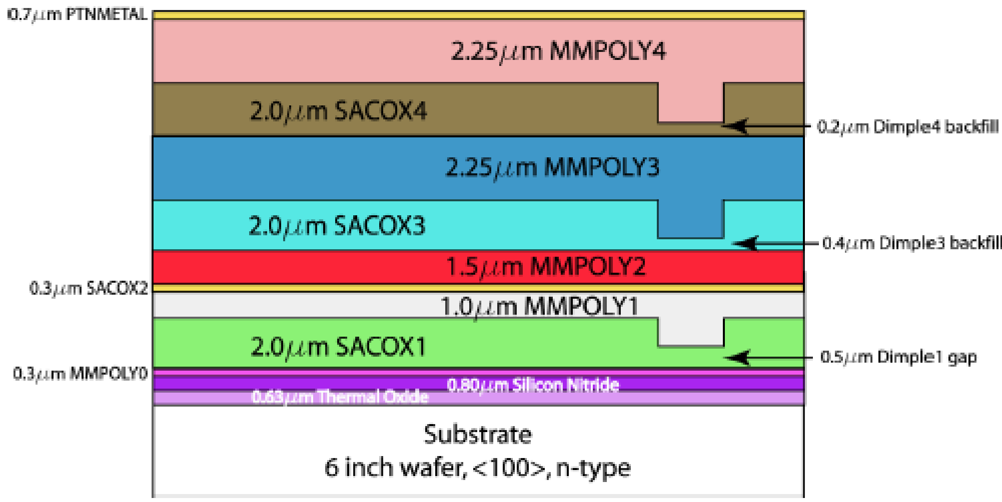

Fig 3.1Drawing of the SUMMiT V structural and sacrificial layers, from ref [26]

There are two types of "CUTS" offered for patterning layers. The first one normally intended to anchor one layer of polysilicon to the polysilicon layer immediately below it and called "Anchor Cut". The anchor cuts are basically regions in oxide or polysilicon layers that etched all the way through to the polysilicon or oxide layers respectively. The other type of cuts called" DIMPLE Cut". Dimple cuts are similar to anchor cuts, but they do not physically anchor to the underlying layer. The only dimple cut we used is performed by timed etch designed to stop after penetrating 1.5μm into 2μm SACOX1, leaving 0.5μm clearance beneath the dimple. Sandia offers an alignment tolerance of 0.5μm in the worst case. This margin has to be taken in the design consideration.

3.2 FABRICATION OF THE DEVICE

We start off with 0.3μm thick Poly0 layer (Purple) composed of polysilicon deposited on a silicon wafer with 0.6μm layer of thermal oxide and 0.8μm silicon nitride deposited on it (Grey) and patterned to divide the regions on which the voltage will be applied from those regions which will be grounded Fig3.2. The electrodes are 60μm×6μm rectangles with rounded edges (to prevent unwanted electrical effects). The electrodes of the same column are wired together with 3μm thick lines that are also created at this stage. The grounded regions around the electrodes are going to act as electric shields so that when voltage is applied on one electrode the other electrodes will not accumulate electric charge. Since the next oxide layer is 2μm thick the cuts may be as wide as 3.5μm so that the next oxide layer will fill the gaps in the polysilicon layer and create a uniform layer of oxide above it (with small insignificant sags in the oxide layer).

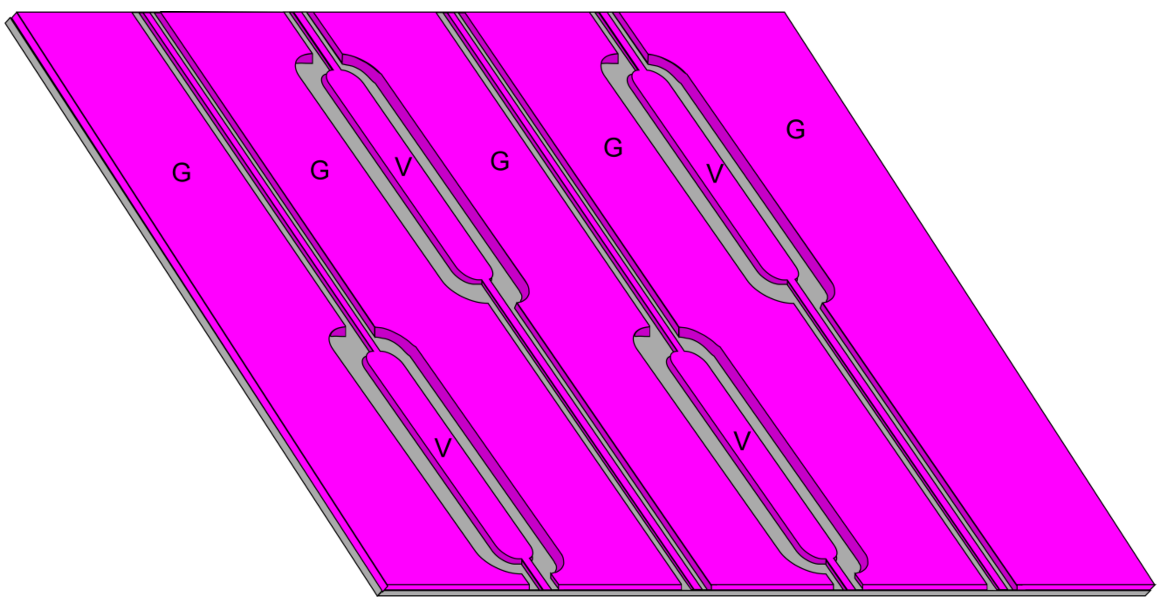

Fig. 3.2 MMPOLY0 deposition and patterning.

2μm oxide layer is deposited and patterned (Green, Fig. 3.3) to raise the actuator above grounded shield but not above the electrode or spring anchor points. We also create small cuts to create a tunnel to bury the wiring of the electrodes. Those cuts are narrow enough (1μm) so that the next MMPOLY1 layer will fill the cuts in the oxide and yet to create as uniform as possible polysilicon layer MMPOLY1.

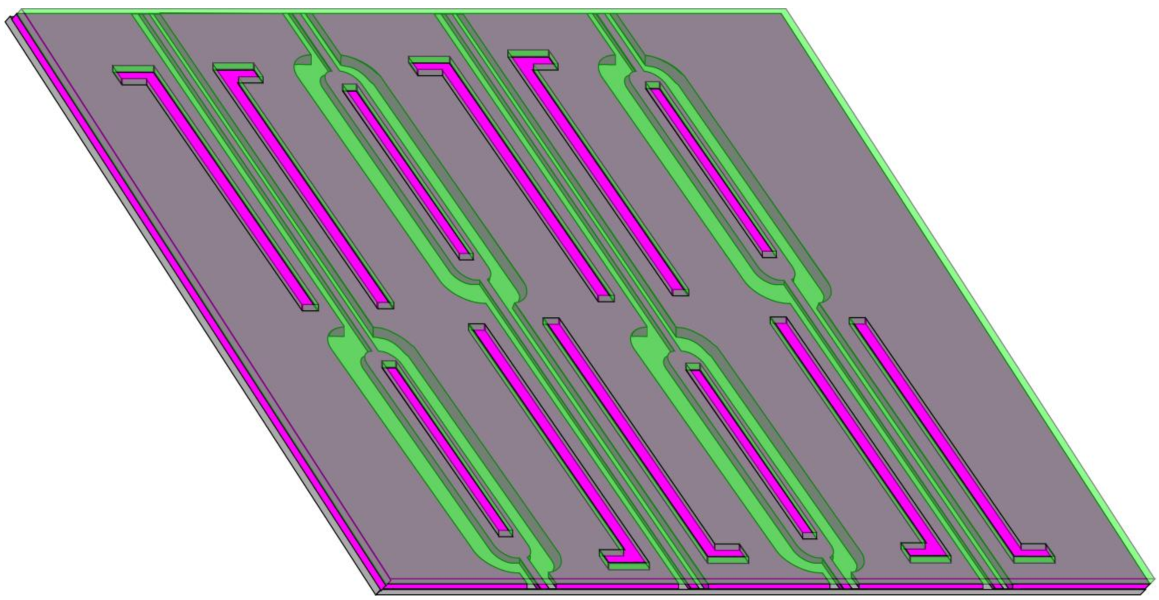

Fig. 3.3 SACX1 deposition (Green) and patterning.

In the next stage 1μm×1μm dimple cuts (Fig. 3.4) are made to create dimples in the middle of the spring. This dimple will create the nonlinear spring that will significantly increase the pull-in voltage and will prevent the structure from snapping down.

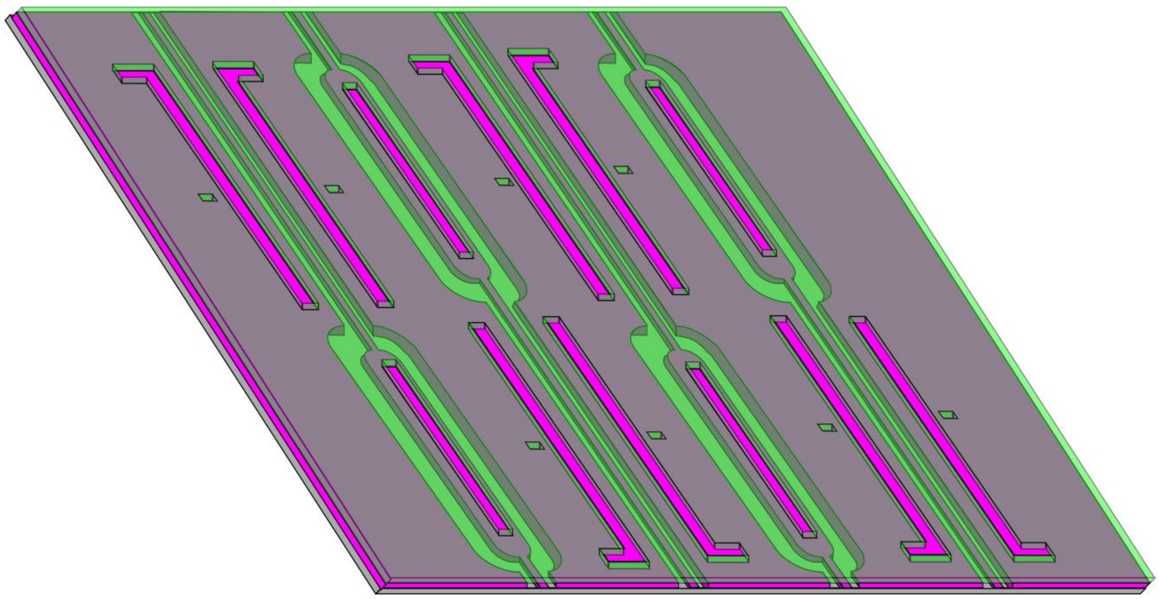

Fig. 3.4 DIMPLE CUT1 is performed.

In the following stage 1μm thick MMPOLY1is deposited (White Fig3.5). This polysilicon layer is not patterned at this stage, but it will be cut along with the MMPOLY2 layer. This way the misalignment problem that may have appeared if each of the layers was patterned individually is eliminated.

This next 0.3μm thick SACOX2 layer is deposited (Orange, Fig. 3.5), creating a mask for MMPOLY1. The regions in MMPOLY1 that are covered by this oxide or by MMPOLY2 will be etched away. The regions that will be covered by MMPOLY2 but not by the SACOX2 will not be etched away but those regions will be connected to the MMPOLY2 layer. We are interested to create the electrode (rectangles with rounded edges), spring (70μm×2μm beams connected at the end to a rectangular plate) and the wire tunnel (rectangular plate covering the wire) only in MMPOLY1. The actuator should be connected to the MMPOLY2 layer that region is not covered completely but still covered on the edges due to misalignment issues to insure a clean cut. Rectangular 62μm×1μm holes are left to connect between MMPOLY1 and MMPOLY2.

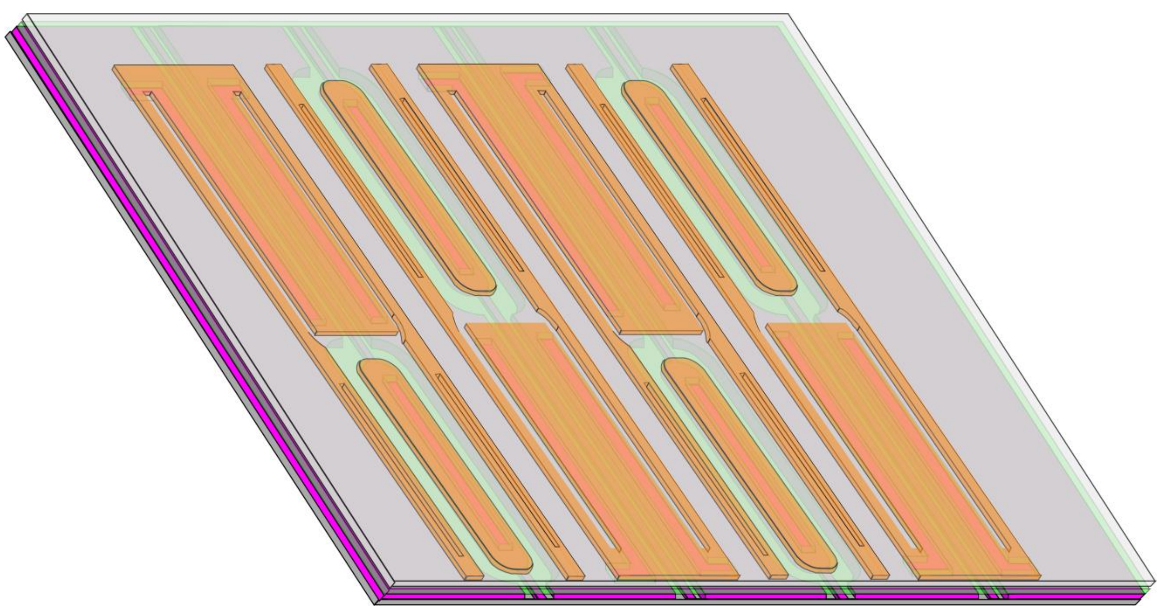

Fig. 3.5 MMPOLY1 is deposited (White). SACOX2 mask layer is deposited (Orange)

In this next stage 1.53μm thick MMPOLY2 (Red, Fig3.6) is deposited and patterned. As mentioned earlier, only the unprotected regions are etched away. Now the electrodes, springs and wire protecting tunnels are complete. 66μm×2.5μm beams created in MMPOLY2 are used to elevate the actuator and to create sufficient gap between the electrode and the actuators upper part. This gap will enable the desired motion range.

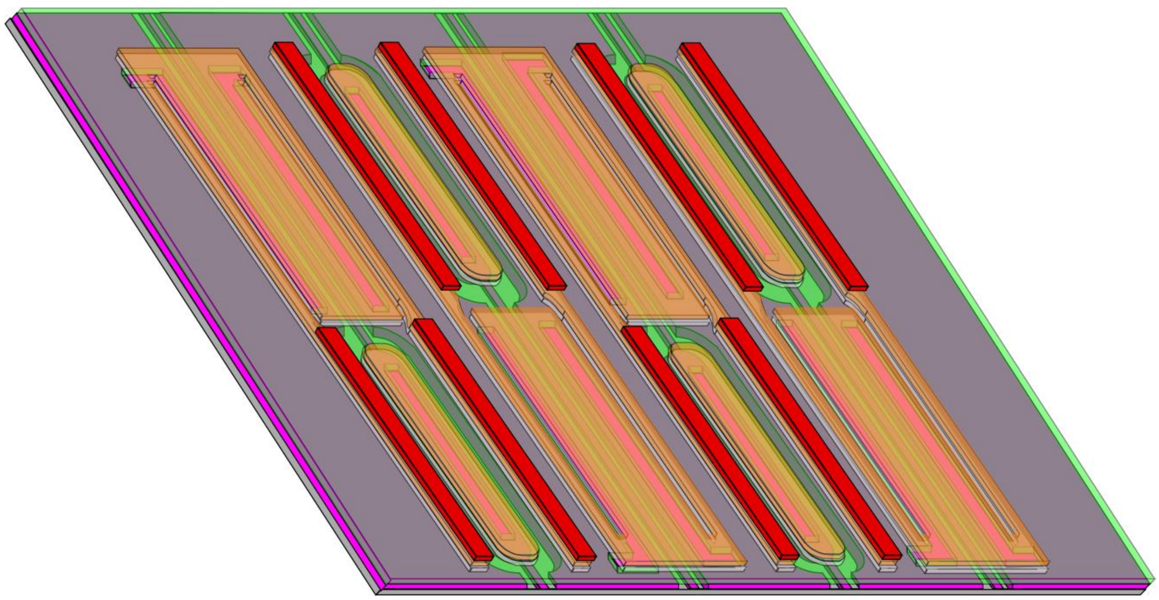

Fig. 3.6 MMPOLY2 is deposited (Red) and patterned along with MMPOLY1.

The following stage 2μm thick SACOX3 (Pale Blue, Fig. 3.7) is deposited, planarized and patterned. In this stage the oxide deposited than planarized to the desired 2μm thickness above MMPOLY2 level, using a CPM process. That way at the end of SACOX3 deposition we get a smooth oxide surface and all the topography created by previous layers is filled with oxide. After the planarization, 62μm ×1μm anchor cuts are made above the MMPOLY2 beams to connect between the following MMPOLY3 layer to the structure underneath.

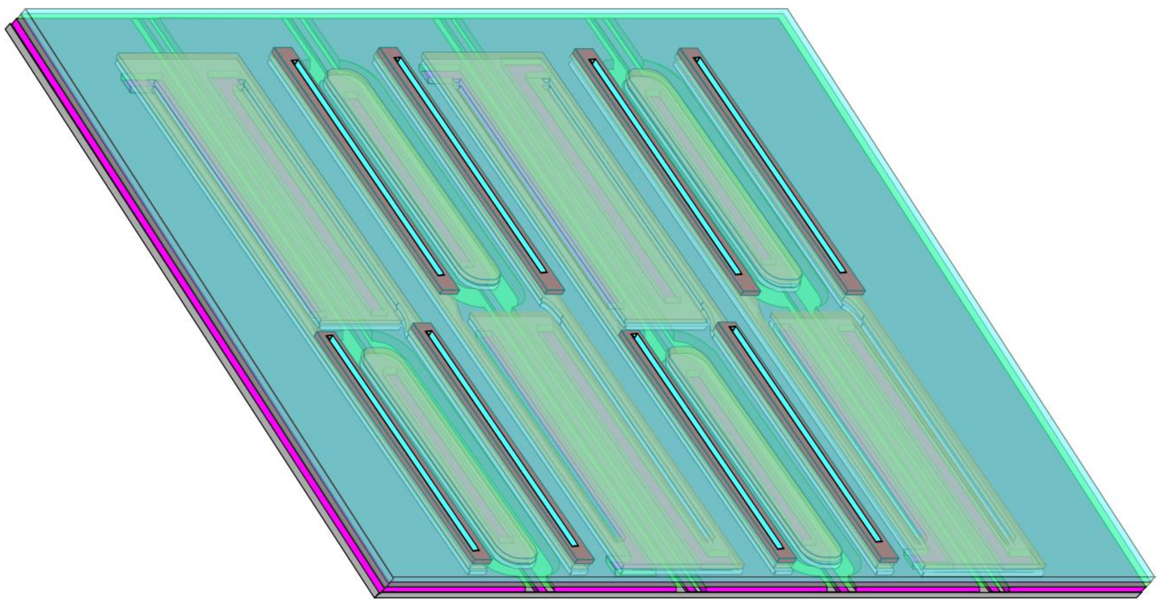

Fig. 3.7 SACOX3 deposited, planarized and patterned.

The next stage is deposition and patterning of 2.25µm MMPOLY3 (Blue, Fig. 3.8) forming long beams that are connected to MMPOLY2 only in the electrode regions. This layer is completes the actuators by forming a box above the electrode. The planarization of the underneath SACOX3 layer insures that beam part that serve as the upper plate of the actuator is smooth and parallel to the electrode surface which is critical for the actuator performance. Each beam is connecting all the actuators of the same column together and turn separate structures into one structure with multiple electrodes and multiple springs. This will insure that all the mirrors connected to the column move together.   Etch release holes are made in the structure to make it easier for hydrogen-fluoride (HF) to penetrate into the structure. The etch release holes will have to be placed 38 µm apart for uniform release. HF is used in a later stage to etch away all of the remaining oxide. Easy access of HF into the structure insures that the structure will be successfully released.

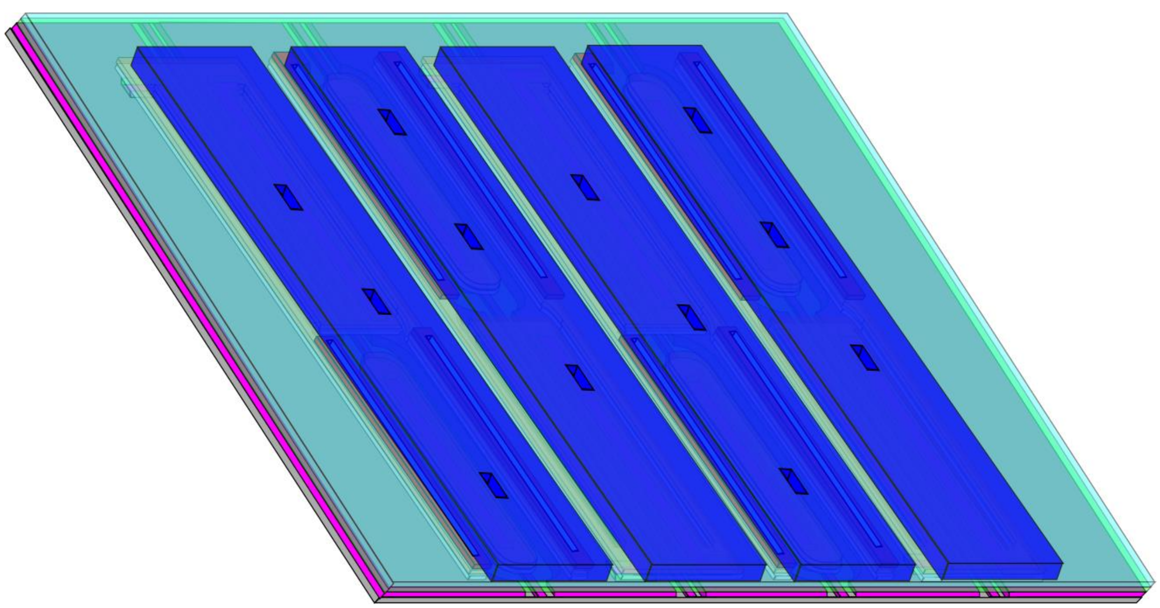

Fig. 3.8 MMPOLY3 deposited and patterned.

The last 2µm thick oxide layer (SACOX4, Light Purple, Fig. 3.9) is deposited, planarized and patterned. Similarly to SACOX3 the topography created by MMPOLY3 is filled with oxide and the upper surface of the layer is polished CMP process. The polishing of the SACOX4 layer insures that the above layer will be flat which is critical since the above layer will form the mirrors. Cuts are etched to anchor the mirrors to a lower polysilicon layer. Those cuts have to be as narrow as possible to insure the flatness of the mirrors that will be deposited above, yet the cuts has to be big enough to hold the mirrors in place. The cuts are designed to be narrow rectangles. This way the anchor is strong enough because the area of the rectangle is relatively large on one hand and narrow enough to be filled without leaving significant topography in the mirror layer on the other hand. Every two actuator beams form a single column of mirrors. The cuts are designed to connect every second mirror in the column to same beam/actuator. This way all even and odd mirrors of the same column may be actuated independently.

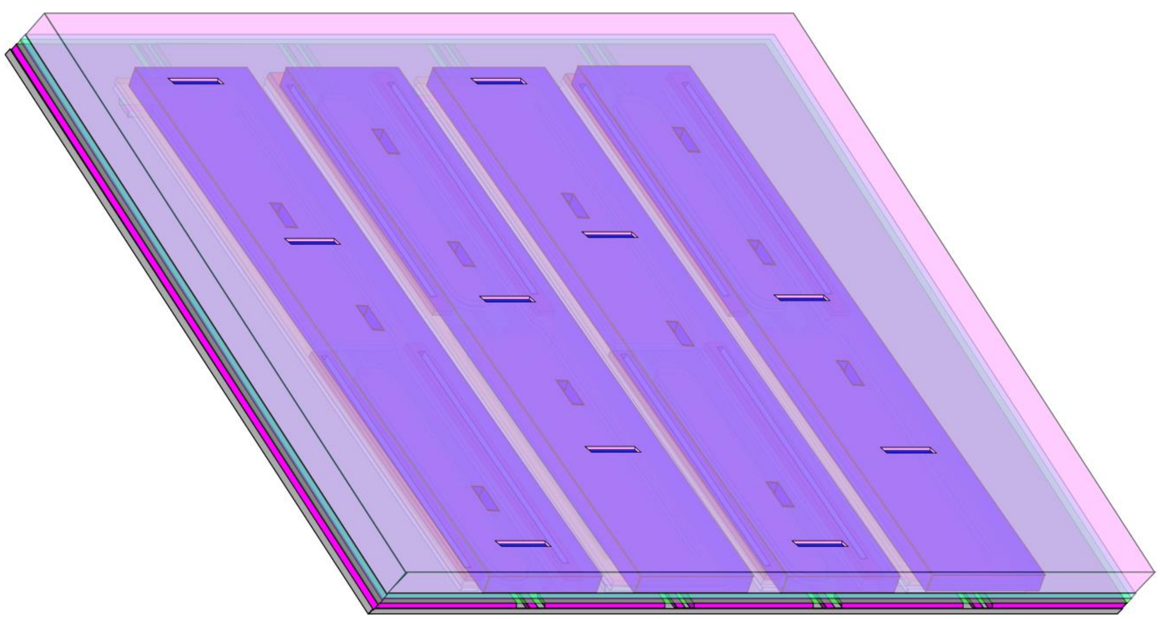

Fig. 3.9 SACOX4 deposited, planarized and patterned.

The last layer deposited is 2.25μm thick MMPOLY4 (Fig. 3.10, Dark Purple). This layer is used to construct the mirrors. The mirrors are 36 μm ×36μm squares with 1μm gap between them.

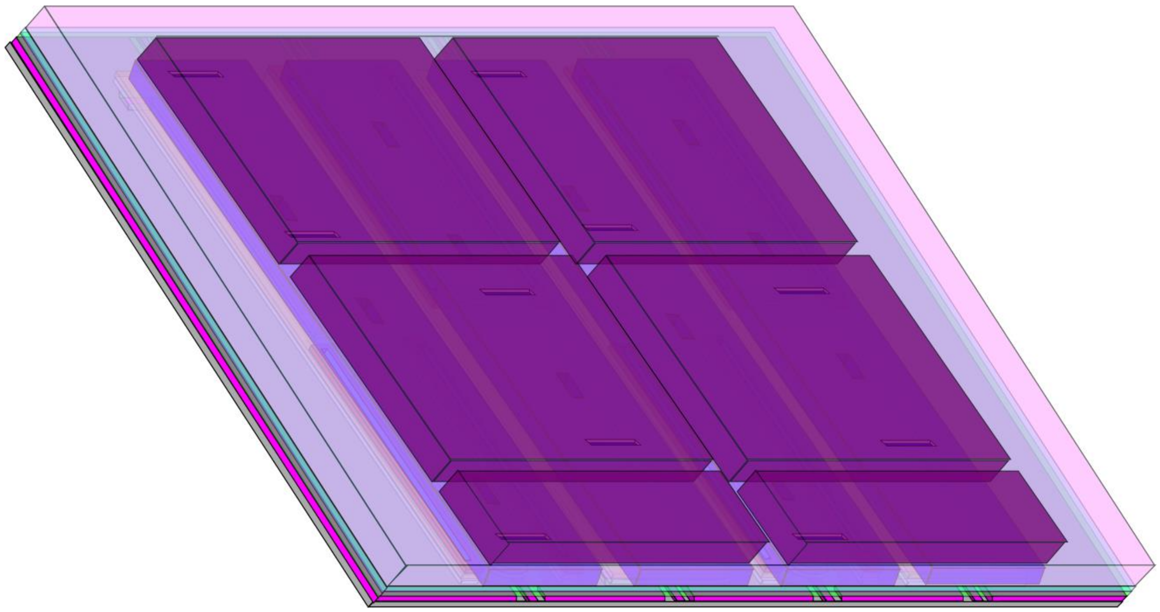

Fig. 3.10 MMPOLY4 deposited and patterned.

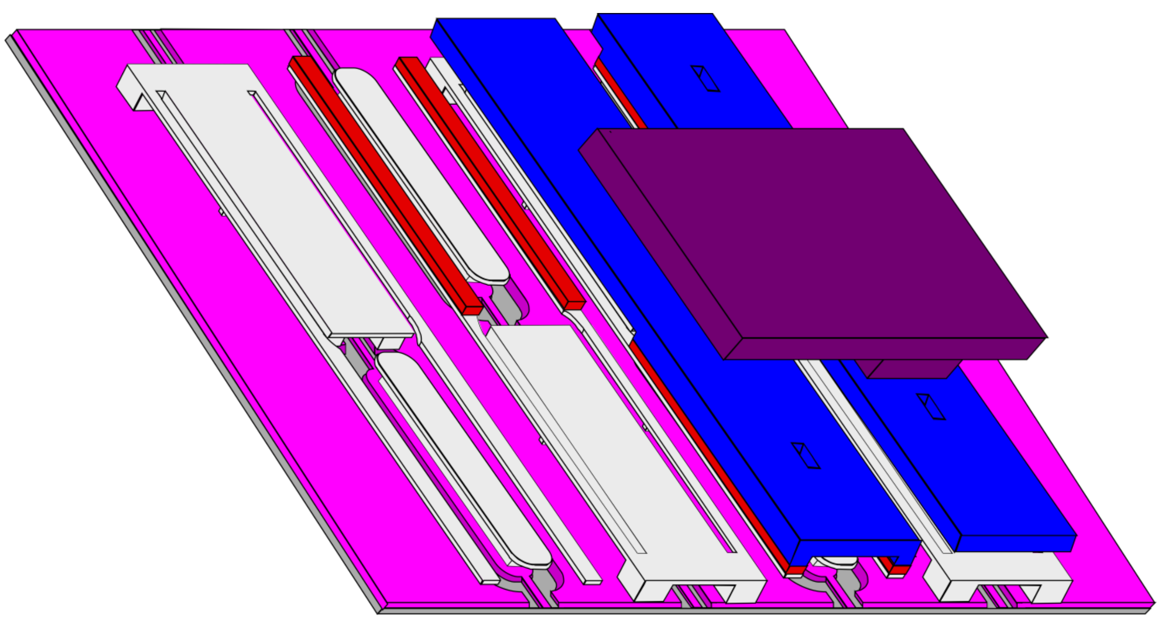

Fig. 3.11 The released structure shown layer by layer from left to right. MMPOLY0+MMPOL1 is first on the left, MMPOLY0+MMPOL1+MMPOLY2 is second on the left, MMPOLY0+MMPOL1+MMPOLY2+MMPOLY3 is third on the left and the final structure is shown on the right.

After all the SACOX and MMPOLY are deposited and patterned, the structure gets a HF wet etch. HF etches all the exposed sacrificial oxide leaving only polysilicon behind. The released structure is shown in Fig. 3.11. The oxide inside the tunnels that cover the wires is not etched. Since this tunnels designed for electric shielding or basically to prevent from the charged wires to apply attractive force on the springs, the oxide does not bother the moving structure.

3.3 POSTPROCESSING

The MEMS device is designed for optical communication wavelengths (c band: 1530nm-1561nm). The problem is that polysilicon does not reflect those wavelengths very well. There is a need for reflective coating. Sandia offers metallization as part of the process, which is optimized for bond pads; a 700nm Au layer on 15nm Cr layer (an adhesion layer). However as a mirror reflective coating, this metalization stress issues when deposited on polysilicon due to a big coefficient of thermal mismatch which would form curvature on the mirrors. The second reason is that 700nm of Au is too thick and heavy, which would decrease the natural frequency of the system dramatically. A custom metallization process was developed in order to cover the mirrors with Au after the release. I used 5nm of Titanium as an adhesive layer to cover it with 50nm of gold. That is thick enough for reflecting the c-band wavelengths on one hand and thin enough to allow low stress deposition.

I designed a custom process that enables the metallization using a shadow mask. The shadow mask is a 50µm thick stainless steel plate with accurate cuts made by a laser. The regions on the chip that need to be coated are opened the mask while the regions that have no need for gold coating remain. The masks are commercially available at SURON A.S.A L.T.D. The mask is glued into an adapter that was also custom made. The adaptor is needed to match the mask size to the mask-aligner's vacuum holder. I used a Suss MA06 mask-aligner. The chip (Green, Fig 3.12) is attached to the two small stages (Red) made on a 2" chip holder using adhesive tape. The upper part of the chip holder that has a hole slightly wider than the chip's width then screwed in forming a 2" plate with the chip held inside it so that the chip's upper level is 100µm lower than the upper level of the chip holder. The mask is then aligned using the mask-aligner through the cuts in the mask. Special alignment marks were made on the chip to ensure more accurate alignment. After the chip and the mask are aligned I bring the mask and the chip holder into contact and place UV adhesive in the small holes made in the mask adapter. The adhesive reaches the upper part of the chip holder. I illuminate all this structure with UV light which hardens the adhesive. Right after the UV illumination, the vacuum in the mask aligner has to be turned off to release the mask from the aligner. Now I have a chip held inside the chip holder aligned and covered by the mask. All this structure goes into VST TFDS-141 evaporator. 5nm of titanium is deposited for the adhesion layer followed by a 50nm gold layer. After the structure is covered with gold and cooled I open the screws in the chip holder so that the lower part of the chip holder and the chip remain in one hand while the upper part of the plate along with the mask and its adapter is in the other. This way the mask is aligned and removed without actually touching the chip. All that is left now is to move the chip from the stage back to its gel-pack.

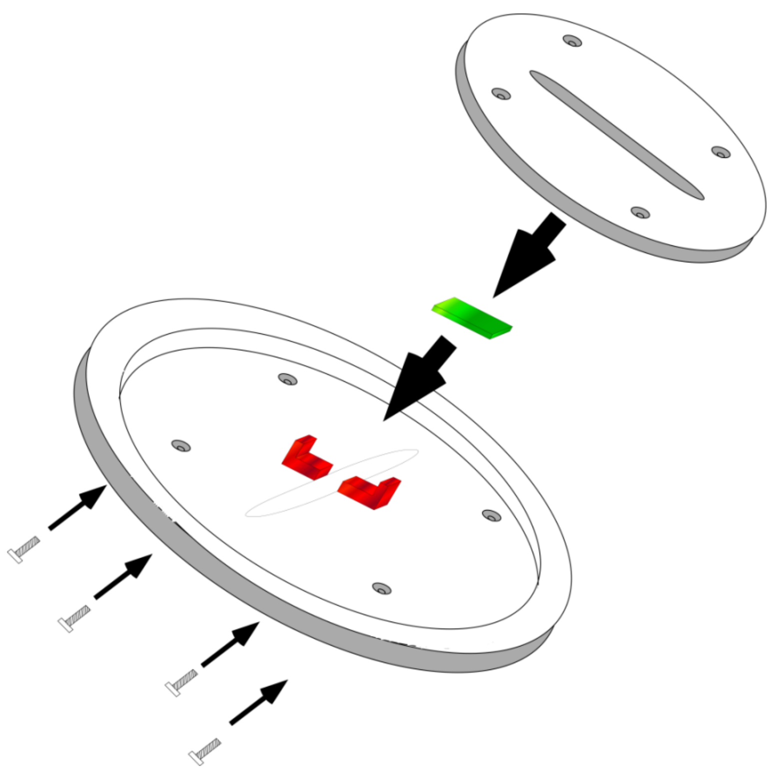

Fig. 3.12 Chip holder. Chip stage (Red) and the chip (Green)

3.4 PACKAGING

I glued the chip to a commercially available ceramic carrier. The bond pads on the chip were wire-bonded to the pads on the carrier. The carrier is then plugged into a socket that is hard-wired to a DAC controller controlled by a computer. This way I can apply different voltages on different pins of the carrier simultaneously without a need for multiple power suppliers.

CHAPTER IV

RESULTS

This chapter describes the characterization and the performance of the fabricated device. The displacement versus voltage characteristics of the fabricated device is presented. The method for measuring the natural frequency of the device is presented along with the obtained results. The optical measurement methods are presented in this chapter along with optical results that demonstrate the functionality of the device for optical communication applications.

4.1 DEVICE OVERVIEW

The fabricated chip is presented in Fig.4.1. The modulator is composed of a two dimensional micromirror array, consisting of 12 columns along the dispersion axis and 33 mirrors in the orthogonal direction. The dimension of each micromirror is 36µm×36µm, with 1µm gap between the mirrors. Overall the fill factor is 94.35%. There are24 actuators underneath the mirrors, two actuators underneath each column. Each actuator is connected to the bond-pad with 3µm wide conductive trench. Each bond-pad is 200µm×200µm gold covered squares with 308µm pitch.

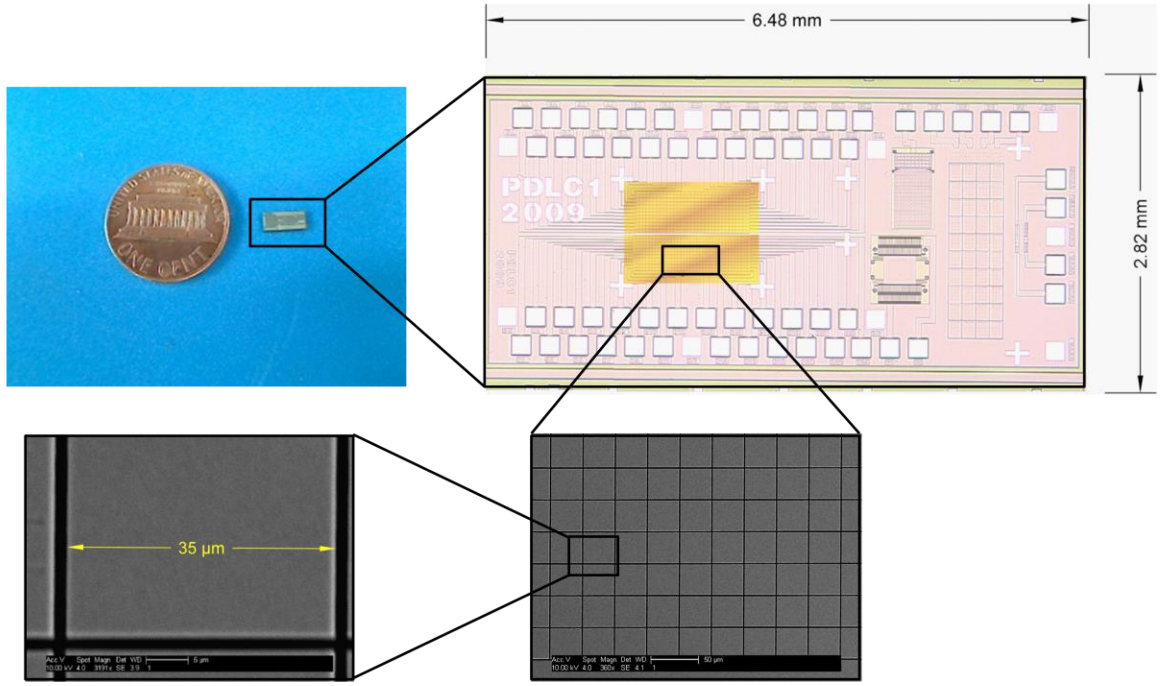

Fig. 4.1A microscope picture of the fabricated chip. The white squares on the top and bottom of the chip are the bond-pads. Gold painted region is the mirror array area. Conductive tranches connecting the bond-pads and the mirrors.

4.2 DIRECT MEASUREMENTS OF ELECTROMECHANICAL PERFORMANCE

We have used an interferometric microscope to measure the relative displacement in a single column. We applied 0-130 volts on the device. The measurements are shown Fig.4.2. The measurements show that we need as much 80 volts for the desired 800nm displacement, as predicted in the design phase.

It seems from the measurements (Fig. 4.3) that the even and odd mirrors are slightly displaced (about 100nm). This might be caused by the fact that the legs of the even and odd mirrors are pointed in different directions. The stress that is applied on the substrate that was created while gluing the chip to the ceramic carrier might be the cause of this displacement.

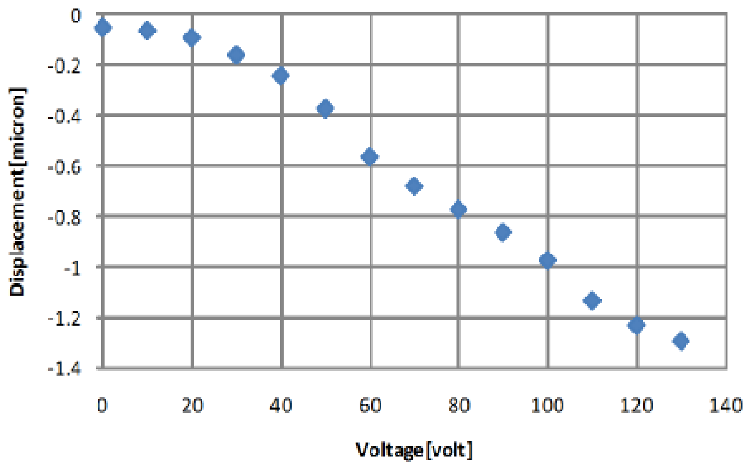

Fig.4.2 A graph showing voltage vs. the relative measured by an interferometric microscope. The measurements were taken in respect to a neighbor mirror.

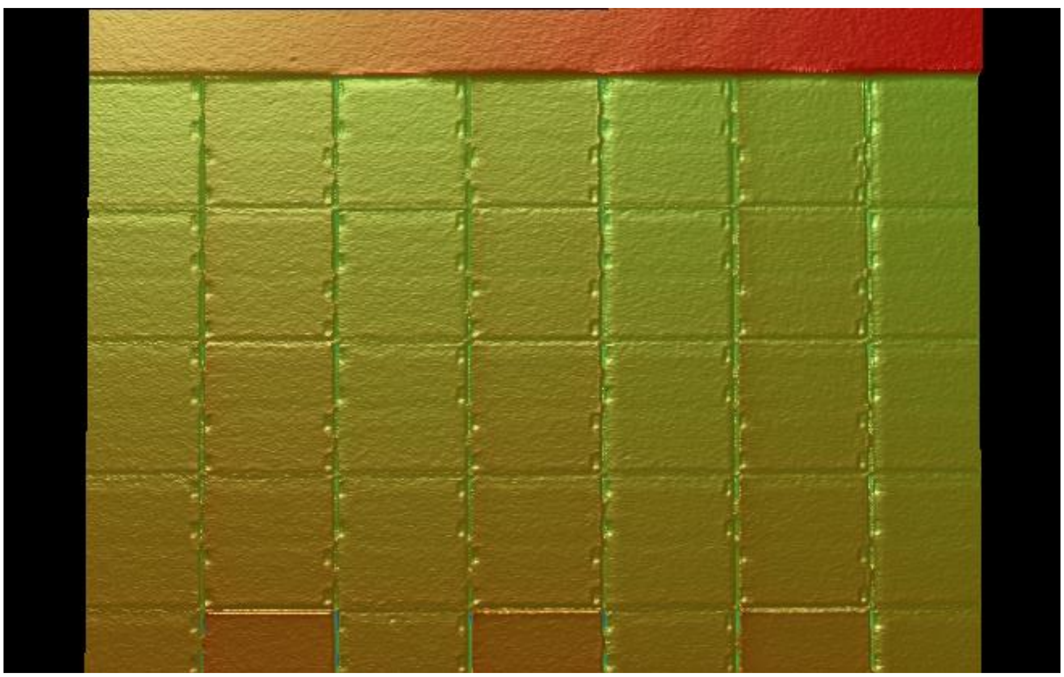

Fig.4.3 Image of the MEMS SLM with no voltage applied. Image was taken by WYKO interferometric microscope.

Fig. 4.2 doesn't look like the Comsol simulation displacement-voltage graph (Fig. 2.7). It gets a linear like behavior around the pull-in voltage and not a sharp edge as was predicted by the simulation (Fig.2.9). We believe that it is a results of the fact that dimples (Fig.2.8) of the column that are created to prevent sticktion do not touchdown on the substrate simultaneously due to the stress that apply on chip and curve it a bit. That makes the stiffness transition smoother.

A single mirror radius of curvature was also measured by an interferometric microscope to determine the flatness of the mirror. A single mirror radius of curvature was measured to be over 300mm.

Relatively stiff springs result in a large enough restoring force to overcome Van Der Waals forces. Dimples in the middle of the spring not only ensure that the structure can only touchdown on few discrete points but also dramatically increase the stiffness of the spring the moment the dimples touchdown. We have applied more than 200volts on a single column. The structure restored its position the moment we shut the voltage down.

4.3 OPTICAL MEASUREMNTS

The experimental setup presented in Fig.4.4 was assembled to test the amplitude and phase response of a single column modulator. Light with wavelength of 1550nm from a laser, passes through an optical circulator, collimated by the collimator and split by a beam-splitter. One beam goes to reference mirror while the other is going through a cylindrical lens and gets focused on one column of the MEMS SLM. After the manipulation that was performed by the MEMS SLM, both beams get reflected back through the beam splitter and coupled back to the fiber, through the circulator and to a power detector.

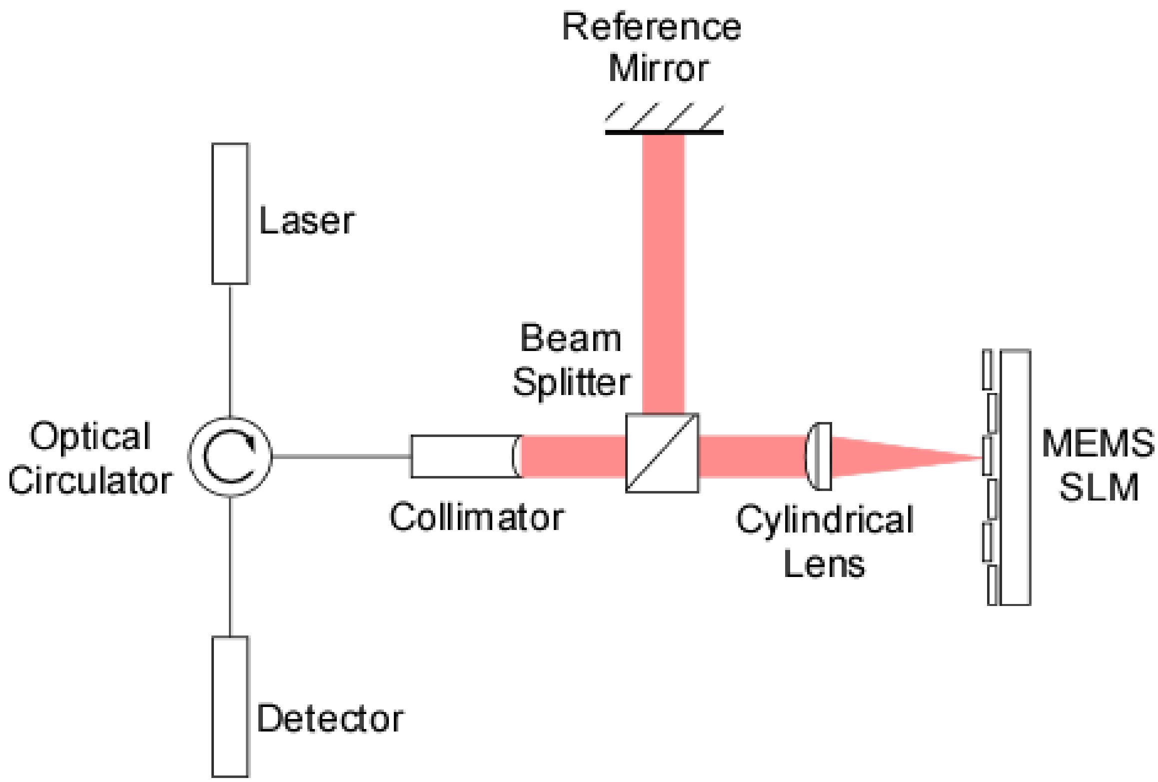

Fig.4.4 An experimental interferometric setup.

The first thing that can be done with that sort of measurement setup is to cover the reference mirror and measure the power of the reflected light. We illuminated one column of the MEMS chip with 1550nm light through a circulator and detected the intensity of the reflected beam, while actuating only the even pixels of that column with a square wave. Different locations of the even pixels of that illuminated column correspond to deferent intensities of the reflected light that is detected. We have basically measured the step response of the even mirrors of one particular column. The measured curve was analyzed by differentiating it and applying a Fourier transform on it. This way the frequency response curve was derived (Fig.4.5). The resonant frequency we observed is 24.2KHz and Q-factor was calculated, Q=1.4.

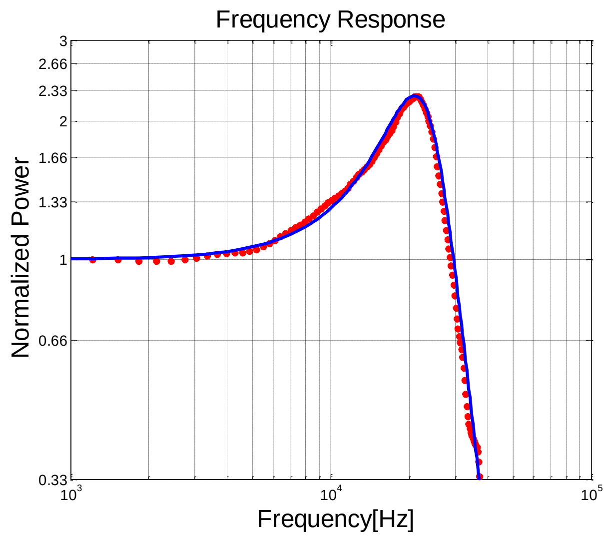

Fig.4.5 A graph showing the mechanical frequency response of a single actuator. Blue curve is theoretical fit and red marks is experimental data.

This experimental setup was this used to measure the phase and the amplitude that is prescribed by the SLM. When the setup is as presented in Fig.4.4, the power of the interference between the light that is reflected from the reference mirror and from the SLM is detected, providing information about the optical phase. If we block the path to the reference mirror no interference occurs and the power that is measured is a measure of the amplitude of the reflected light. All combinations of voltages from 0-100volts were applied on the odd/even mirrors of one mirror column. An analytical calculations was created to compare the result with theory. Fig.4.6 shows the analytical calculations and measurement for detected power in the interferometric phase and intensity only measurements. The x-axis is the odd mirror displacement and the y-axis is even mirror displacement. Z-axis represent the normalized power that detected. We see that the measured results well match the simulations. Full 2π phase modulation was also witnessed. Power that is measured is a good indication for amplitude of the reflected light. The simulation is based on simple calculations. When the reference mirror is covered, only the zero order of diffraction is detected. The phase of the reflected light from each mirror depends on it position.

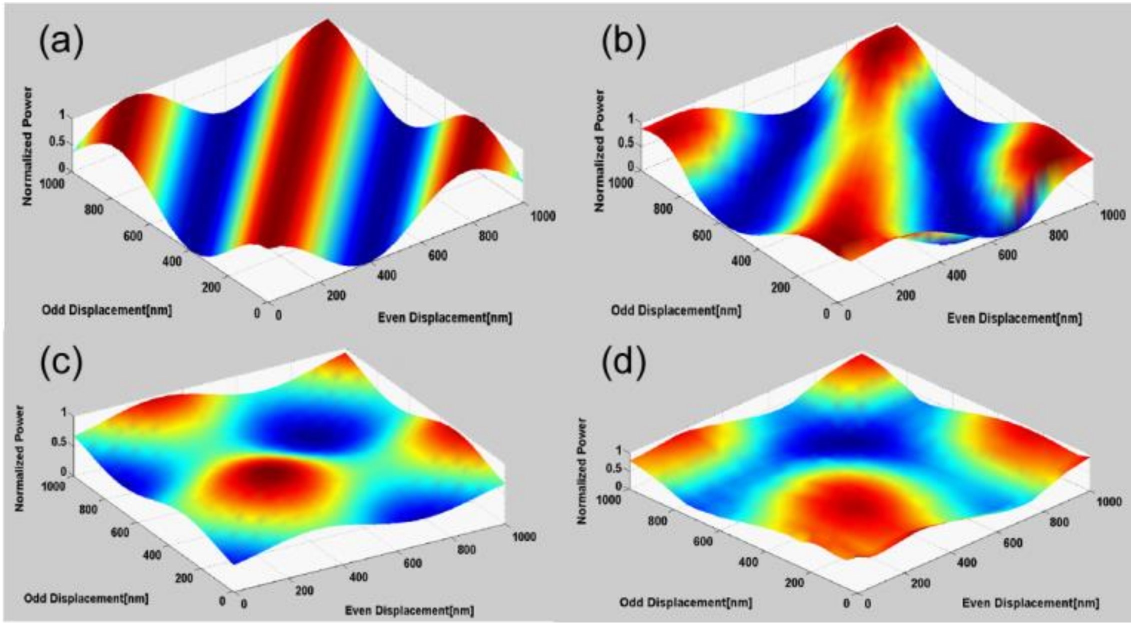

Fig.4.6 An experimental setup result and the analytical calculations. (a) and (b) are the simulation and a measurement respectively of the experimental setup with blocked reference mirror that indicates the amplitude of the light reflected from the SLM. (c) and (d) are the analytical calculations and a measurement respectively of the experimental setup as presented in Fig. 4.3 that indicates the phase measurement.

The dependence between the phase of the incident light and the displacement is: $\phi = \frac{4\pi d}{\lambda}$,where ϕ is the phase, d is the displacement and λ is the wavelength of the incident light. The field expected to be detected is:

$$S = A_s exp\left[j\left(\frac{4\pi d_{even}}{2\lambda} + \frac{4\pi d_{odd}}{2\lambda}\right)\right] cos\left(\frac{4\pi d_{even}}{2\lambda} - \frac{4\pi d_{odd}}{2\lambda}\right),$$

where S is the detected field, A_s is the amplitude of the field.

The power that is expected to be detected is:

$$Power = |S|^2 = A_s^2 cos^2\left[\frac{2\pi(d_{even}-d_{odd})}{\lambda}\right]$$

That function is illustrated in Fig.4.5a. So in fact the detected power should be a function of the difference between the even mirror displacement and the odd mirror displacement only. In other words, $Power(d_{even}, d_{odd}) = Power(d_{even} - d_{odd})$.

When the reference mirror is uncovered, the second beam interferes with the reflected light (the one that comes from the reference mirror). The field that is reflected from the reference mirror: $R = A_r exp(j\theta)$ where A_r is the amplitude and θ is the phase of the beam that is reflected from the reference mirror. This time the detected power is composed of two fields, the reference and the zero order of diffraction from the MEMS SLM. So the detected power is $|S + R|^2$. The full expression of the detected power is shown below.

$$Power = A_s^2 cos^2 \left[\frac{2\pi(d_{even} - d_{odd})}{\lambda}\right] + A_r^2$$
$$+ 2A_s A_r cos\left[\frac{2\pi(d_{even} - d_{odd})}{\lambda}\right] cos\left[\frac{2\pi(d_{even} + d_{odd})}{\lambda} - \theta\right]$$

That function is illustrated in Fig.4.6c. Again we see excellent correspondence to the measurements in Fig 4.6d.

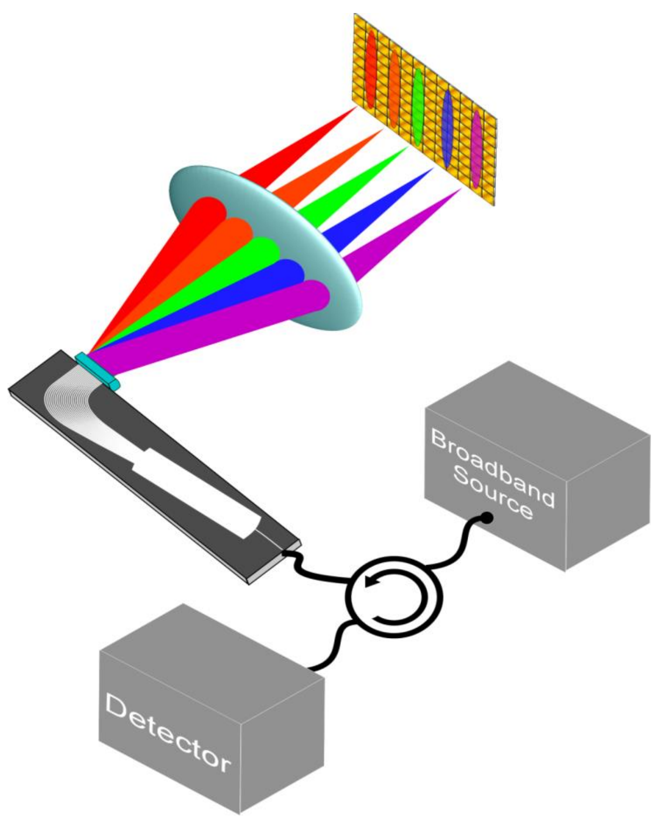

Fig. 4.7 –The light comes out from the arrayed waveguide grating (AWG) is being dispersed and broadened by the cylindrical lens, different wavelength components focus on different lateral positions on the MEMS SLM plane, and then can be manipulated with the phase MEMS SLM. In the black box – the spot from the SLM point of view, the elliptic shape is due to the cylindrical lens.

The optical setup that was used to demonstrate the signal processing abilities is shown in Fig. 4.7. Light from a broadband source via optical circulator enters a planar lightwave circuit (PLC) containing an array waveguide grating (AWG) through the “I/O” waveguide. The angular dispersion at the end of the PLC is then converted to a lateral one with a Fourier lens, resulting in a spatial distribution along x- axis. A cylindrical lens is attached to the PLC in order to collimate the radiating light in the vertical direction (non-information carrying). The light reaches the MEMS SLM. Each spectral component gets manipulated independently and reflected back to the optical circulator's outport to be detected at the LUNA Optical Frequency Domain Reflectometer (OFDR).

The attenuation of spectral component was tested by applying different voltages on one actuator which pulls one set of even mirrors of a single column. This way spectral component that falls on that column is attenuated. The level of attenuation depends on the phase difference between the even (actuated) mirrors and the odd (not actuated) mirrors of that column. Fig.4.8 shows levels of attenuation for each phase difference.

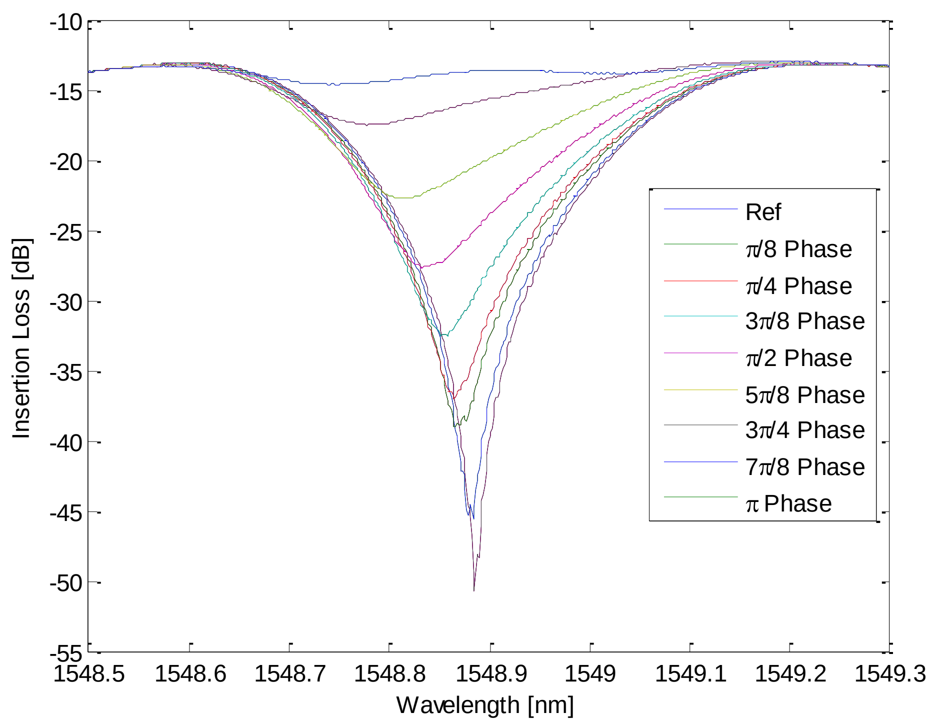

Fig.4.8 – Demonstration of phase step applied with one column. The maximum attenuation achieved at a phase difference of π is -38dB.

Next the ability of the device to block different spectral components was tested. Voltage that corresponds to π phase difference was applied each time only on the odd mirrors of different columns. The result is presented in Fig.4.9,4.10 It can be seen each time a different spectral components gets blocked.

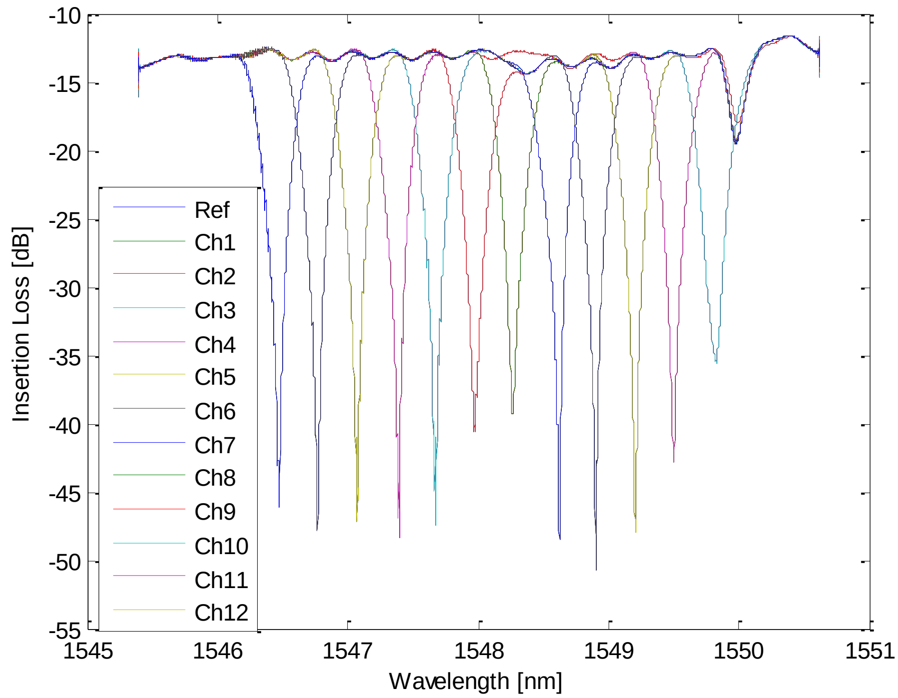

Fig.4.9 – Demonstration of phase step applied on each column. Spectral components get blocked one by one.

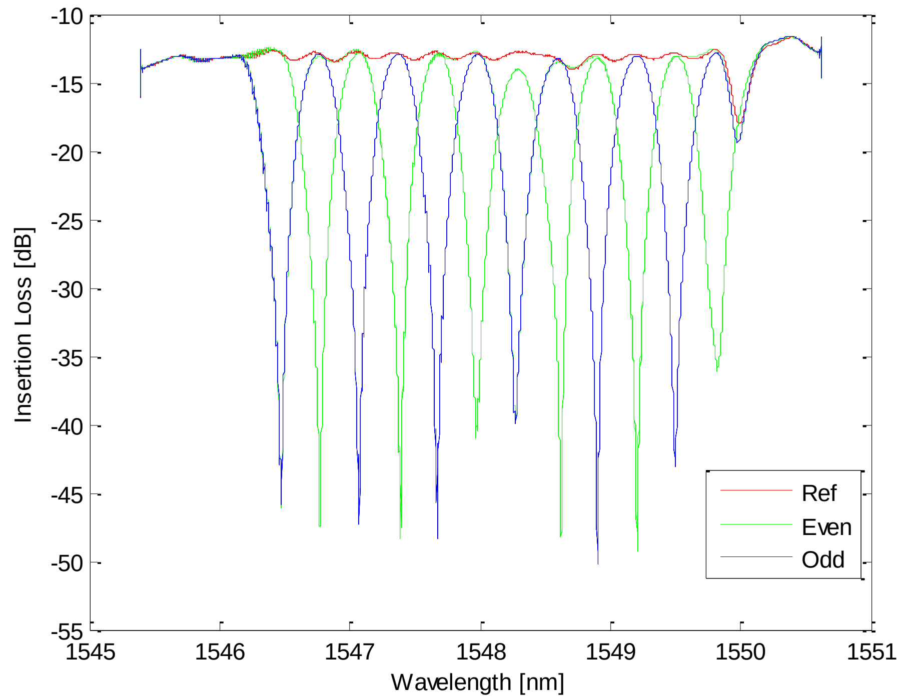

Fig.4.10 – Demonstration of phase step applied on six spectral components at a time. Six odd channels (blue) and six even channels (green) . The reference with no blocked spectral components is presented in red. Spectral components get blocked.

To test the MEMS SLM's Tunable Dispersion Compensation performance, quadratic phase functions with varying radii were applied in the dispersion direction. The group delay results shown in Fig.4.11. The chromatic dispersion values are listed in the table 4.1.

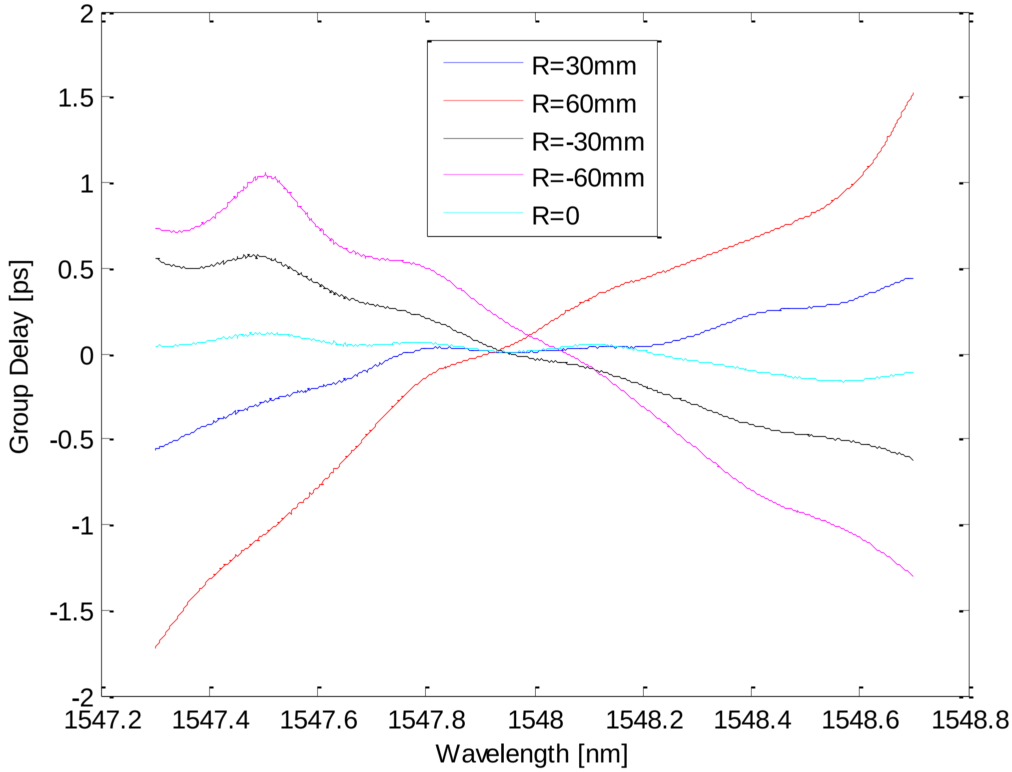

Fig.4.11 Quadratic phase (chromatic dispersion compensation) results. Group delay versus frequency. Linear slopes are observed, corresponding to four different dispersion values

Radius of Curvature [m]	Calculated [ps/nm]	Measured [ps/nm]
0.03	1.033	0.714
-0.03	-1.033	-0.963
0.06	2.07	2.32
-0.06	-2.07	-1.81

Table 4.1 chromatic dispersion values achieved from Fig. 4.10

The theoretically calculated values were from equation linking the chromatic dispersion (CD) value with the radius of curvature of the reflective mirror.

$$CD = \frac{2\lambda_0}{C_0}\frac{1}{R}\left(\frac{dx}{d\lambda}\right)^2 \qquad (4.1)$$

Where CD is chromatic dispersion, C_0 is the speed of light in vacuum, R is the radius of curvature of the mirror, λ_0 is the central wavelength and $\frac{dx}{d\lambda}$ is the spatial dispersion governed by AWG. The CD values are not high because there are only 12 pixels in the dispersion direction, meaning that high curvatures can't be set.

CHAPTER V

CONCLUSIONS

My thesis describes the design, simulation, fabrication and testing of the MEMS spectral phase and amplitude modulator based on diffractive principles. Particular attention to details was essential to producing a functional device as described in this work.

Electro-mechanical coupling calculations were used in constraints set by the predefined fabrication process to design the MEMS SLM device. The modulator was designed to be scalable to any desirable 2D array size. Comsol FEA software was used to confirm the calculations.

The MEMS SLM device was fabricated at Sandia. The chip consists of 12 columns along the dispersion axis and 33 mirrors in the orthogonal direction. The dimension of each micromirror is 36μm×36μm, with a fill factor of 94.35%. The fabricated device was successfully metalized using our custom metallization method, and was packaged and wire bonded for evaluation and testing.

The MEMS SLM device was tested and the results agreed well with simulations and showed extremely good results in application testing. Displacement up to 1.2 microns was measured. A single mirror radius of curvature was measured to be over 300mm after metallization. The resonant frequency was measured to be 24.2KHz and Q-factor was calculated, Q=1.4. It was shown that the device can achieve any phase and amplitude value independently. The performance of the MEMS SLM in various applications was presented. The device can be used for channel selective applications, for tunable

Wavelength attenuation applications as well as for chromatic dispersion compensation. Maximum attenuation of -38dB was observed which is good for Channel selection applications. The interferometric experiment confirmed that each spectral component can be encoded with any phase from 0 to 2π and amplitude can be controlled almost continuously. Chromatic dispersion performance was presented.

5.1 FUTURE WORK

The current fabricated device showed very nice results for wavelength selective attenuation application but to demonstrate the chromatic dispersion application a bigger array has to be fabricated.

The design of all even column having springs pointed in one direction and all odd having springs pointed in the other direction have created a slight difference in performance between the odd and the even mirrors. In the future I would design all columns to have a identical spring direction to prevent this problem.

REFERENCES

[1] P.F. Van Kessel,L.J. Hornbeck, R.E. Meier, M.R. Douglass, " A MEMS-Based Projection Display," *Procceeding of the IEEE*, vol. 86, no. 8, pp. 1687-1704, August 1998.

[2] K. Sato, M. Shikida, " Electrostatic Film Actuator with a Large Vertical Displacement" , *Micro Electro Mechanical Systems, (MEMS '92)*, Travemund Germany, pp 1-5, February 4-7, 1992.

[3] A. Tuantranont, V.M. Bright, " Segmented Silicon-Micromachined Microelectromechanical Deformable Mirror for Adaptive Optics" *IEEE Journal on Selected Topics in Quantum Electronics*, Vol. 8, No. 1,2002.

[4] T. Bifano, R.K. Mali, J. Perreault, M. Horenstein, D. Koester, "MEMS Deformable Mirrors for Adaptive Optics", *Solid-State sensor and Actuator Workshop*, Hilton Head Island South Carolina, pp. 71-74, June 1998.

[5] M. Hujia, M. Husak, "Thermal microactuators for optical purpose, "*International Conference on Information Technology: Coding and Computing*, pp.137-142, 2001.

[6] J. W. Judi, T. Tamagawa, D. L. Polla, "Surface micromachined linear thermal microactuator, " *International Electron Device Meeting*, pp.629-632, 1990.

[7] M. Ataka, A. Omodaka, N, Takeshima, H. Fujita, "Fabrication and operation of polyimide bimorph actuators for a ciliary motion system," *Journal of Microelectromechanical Systems*, Vol. 2. Pp.146-150, 1993.

[8] M. Pozzi, T. King, "Piezoelectric actuators in micropositioning," *Journal of Engineering Science and Education*, Vol. 10, pp. 31-37, Feb 2001.

[9] H .Toshiyoshi, D. Kobayashi, H. Fujita, T. Ueda, "A Piezoelectric Psuedo-static Actuator for Large Displacement under AC votage operation." *International conference on Solid-State Sensors and Actuators*, 1995. (TRANSDUCERS '95), Stockholm Sweeden, pp.389-392, 1997.

[10] T.Kawabata, M. Ikeda, H. Goto, M. Matsumoto, T. Yada, "The 2-Dimetional Micro Scanner Integrated with PZT Thin Film Actuator, " *International conference on Solid-State Sensors and Actuators*, 1997. (TRANSDUCERS '95), Chicago USA, Vol.1, pp. 339-342, 1997.

[11] H. Toshiyoshi, D. Miyauchi, H. Fujita, "Michromechanical fiber opticsswitches based on electromagnetic torsion mirrors," *IEEE/LEOS Summer Topical Meeting*, pp. II/23-II/24, 1998.

[12] C Lui, T. Tsao, Y.C. Tai, C.M. Ho, " Surface Micromachined Magnetic Actuator'" IEEE Workshop on *Micro Electro Mechanical Systems, (MEMS '94), pp. 57-62, 1994.*

[13] L. Houlet, P. Helin, T. Bourouina, G. Ryne, E. Dufour-Gergam, H. Fujita, "Movable vertical mirror array for optical microswitch matrixes and their electromagnetic actuation," *IEEE Journal on Selected Topics in Quantum Electronics*, Vol. 8, pp. 58-63, 2002.

[14] F. Kawai, P. Cusin, S. Konishi, "Thin flexible end effector using pneumatic balloon actuator," *The Thirteenth Annual International Conference on Micro Electro Mechanical Systems, (MEMS ''2000*), pp. 391-396, 2000.

[15] L.J. Hornbeck "Current status of the micromirror device (DMD) for projection television applications" *Technical Digest, Electron Devices Meeting*, pp. 381-384, 1993.

[16] O. Solagaard, F.S.A. Sandejas, and D.M. Bloom, "Deformable Grating Optical Modulator," *Optical Letters*, vol. 17, pp. 688-690, 1992.

[17] L. Y. Lin, J.L. Shen, S.S. Lee, G.D. Su, M.C. Wu, " Microactuated micro-XYZ stage for free-space micro optical bench," *Tenth Annual International Workshop on Micro Electro Mechanical Systems,(MEMS '97), pp. 43-48, 1997.*

[18] J.E. Ford, V.A. Aksyuk, D.J. Bishop, J.A. Walker, "Wavelength add-drop switching tilting micromirrors," *Journal of Lightwave Technology*, Vol. 17, pp. 904-911, 1999.

[19] H. Chen, C. Chang, J. Chen, J. Chio, K. Yen, F. Xiao, P. Chang, "Fabrication of a Micromachined optical mofulator using the CMOS process," *Transducers '99*, Sendai, Japan, pp. 808-811, June 7-10 1999.

[20] D. Sinefeld and D. M. Marom, “Colorless photonic spectral processor using hybrid guided-wave/free-space optics arrangement and LCoS modulator,” *Opt. Fiber Commun*. (OFC) 2009.

[21] E. Ranalli and B. Scott, “Wavelength Selective Switch,” U.S. Pat. 6 285 500, Sept. 4, 2001.

[22] A.M. Weiner, "Femtosecond pulse shaping using spatial light modulators", *'Rev. Sci.* Instr.71 1929-1960 (2000).

[23] G.Lee, , S. Xiao, , A. M. Weiner, "Optical Dispersion Compensator With>4000-ps/nm Tuning Range Using a Virtually Imaged Phased Array (VIPA) and Spatial Light Modulator (SLM) " *Photonics Technology Letters*, Vol. 18 No. 17, September 1, 2006.

[24] D. M. Marom , D. T. Neilson and D. S. Greywall "Wavelength-selective 1/spl times/K switches using free-space optics and MEMS micromirrors: Theory, design, and implementation", *J. Lightw. Technol.,* vol. 23, pp.1620 2005 .

[25] Hybrid Guided-Wave/Free-Space Optics Photonic Spectral Processor Based on LCoS Phase Only Modulator, Sinefeld, D. Marom, D.M. *Photonics Technology Letters, IEEE* pp. 510 - 512 , Volume: 22 Issue: 7, April1, 2010

[26] http://www.mems.sandia.gov/samples/doc/process.pdf